Helmholtz-Zentrum Dresden-Rossendorf (HZDR)

Magnetic-field-assisted electrodeposition of metal to obtain conically structured ferromagnetic layers

Huang, M.; Eckert, K.; Mutschke, G.;

Originally published:

October 2020

Electrochimica Acta 365(2020), 137374

DOI: https://doi.org/10.1016/j.electacta.2020.137374

Perma-Link to Publication Repository of HZDR:

https://www.hzdr.de/publications/Publ-31638

Release of the secondary publication
on the basis of the German Copyright Law § 38 Section 4.

CC BY-NC-ND

Magnetic-field-assisted electrodeposition of metal to obtain conically structured ferromagnetic layers

Mengyuan Huang[a,*], Kerstin Eckert[b], Gerd Mutschke[a,*]

[a] *Helmholtz-Zentrum Dresden-Rossendorf (HZDR), Institute of Fluid Dynamics, 01328 Dresden, Germany*

[b] *Technische Universität Dresden, Institute of Process Engineering, 01069 Dresden, Germany*

Abstract

Micro- or nano-structured ferromagnetic layers often possess superior electrocatalytic properties but are difficult to manufacture in general. The present work investigates how a magnetic field can possibly support local cone growth on a planar electrode during electrodeposition, thus simplifying fabrication. Analytical and numerical studies were performed on conical structures of mm size to elaborate the influence of the magnetic forces caused by an electrode-normal external field. It is shown that, beside the Lorentz force studied earlier in the case of single cones [1], the magnetic gradient force enabled by the field alteration near the ferromagnetic cathode significantly supports cone growth. Detailed studies performed for sharp and flat single cones allow conclusions to be drawn on the support at different stages in the evolution of conical deformations. Furthermore, the influence from neighboring cones is studied with arrays of cones at varying distances apart. Nearby neighbors generally tend to mitigate the flow driven by the magnetic forces. Here, the support for cone growth originating from the magnetic gradient force is less heavily affected than that from the Lorentz force. Our results clearly show that the magnetic field has a beneficial effect on the growth of ferromagnetic conical structures, which could also be useful on the micro- and nanometer scales.

Keywords:

metal electrodeposition, magnetic field, surface-structured electrode, Lorentz force, magnetic gradient force, numerical simulation

*Corresponding authors.

Email addresses: m.huang@hzdr.de (Mengyuan Huang), g.mutschke@hzdr.de (Gerd Mutschke)

1. Introduction

Conical micro- and nano-structures have numerous applications due to their particular physical and chemical properties which appear when length scales are reduced. Inspired by cicada wings, super-hydrophobic surfaces covered with arrays of conical protuberances were reported to have good self-cleaning properties [2, 3]. For electrochemical applications, nano-structured electrodes are of great importance due to their enhanced catalytic activity. Great efforts have been devoted to increasing the activity of noble-metal-free catalysts by surface nano-structuring in order to replace the rare, expensive Pt-based catalysts widely used in fuel cell technologies [4, 5, 6]. In this respect, conically structured ferromagnetic electrodes have also been reported to reduce the overpotential for the hydrogen evolution reaction by enhancing the active surface area and supporting the bubble detachment [7, 8].

Among the various methods of synthesizing arrays of micro- and nano-cones, electrochemical deposition techniques have been widely applied [9, 10, 11]. As the current density can be expected to be greater at cathode regions closer to the counter-electrode, according to Faraday's law, the deposition rate is higher at e.g. the tip of a cone compared to other flat electrode regions [12]. This mechanism generally supports the growth of non-uniformities during template-free deposition. In order to further enhance a possible structuring effect during deposition, magnetic fields may be utilized. In the past, magnetic fields have already proven a promising tool for controlling the mass transport of the ionic species during electrodeposition processes. A variety of effects can be achieved, among them the enhancement of the limiting current [13, 14, 15, 16], the homogenization of the deposit thickness [17, 18], the modification of the morphology of the deposited layers [19, 20, 21], the reduction of dendrite growth in Li metal batteries [22, 23], and the enhancement of hydrogen evolution in electrolysis [24, 25, 26, 27]. Structured deposits down to the micrometer scale were obtained using planar but magnetically patterned electrodes. Due to the strongly inhomogeneous magnetic field created locally, a correspondingly patterned deposit follows [28, 29]. However, the local modification of the magnetic field during growth of a ferromagnetic elevation has not yet been investigated in detail, which adds motivation for the present study.

It is well known that applying a magnetic field during electrodeposition causes magnetic forces to act on the electrolyte and to drive a flow. These forces are the Lorentz force [13, 30, 31], and possibly also the magnetic gradient force [32, 33, 34]. If the magnetic forces can be designed such as to generate an electrolyte flow which brings fresh electrolyte towards the tip of a cone, local mass transfer would be enhanced and, thus, cone growth would be supported. For the Lorentz force generated by a surface-normally oriented magnetic field, this beneficial effect has firstly been shown near single copper cones [1]. Here, simulations and measurements based on shadowgraphy and Mach-Zehnder interferometry were performed, and a

moderate effect could be observed in a weak magnetic field of 60 mT. The Lorentz force is given by the vector product of the current density $\boldsymbol{j}$ and the magnetic flux density $\boldsymbol{B}$,

$$\boldsymbol{f}_{\mathbf{L}} = \boldsymbol{j} \times \boldsymbol{B} \tag{1}$$

Here, as the electrolyte velocity is usually low ($U \ll 1\mathrm{m/s}$), flow-induced parts of the current density and the magnetic field may safely be neglected [35]. Figure 1(a) schematically shows the flow near a conical cathode driven by the Lorentz force $\boldsymbol{f}_{\mathbf{L}}$ originating from an external magnetic field directed vertically upwards ($\boldsymbol{B}_{\mathbf{0}}$). For diamagnetic and paramagnetic media, there is $\boldsymbol{B} \approx \boldsymbol{B}_{\mathbf{0}}$. Then, the vertical magnetic field and the radial component of the current density caused by the electric field lines bending near the cone surface create an azimuthal flow around the cone [1]. The centrifugal acceleration of the electrolyte away from the cone caused by this primary rotating flow then gives rise to a secondary downward flow which brings fresh bulk electrolyte to the cone tip and enriches the boundary layer [33].

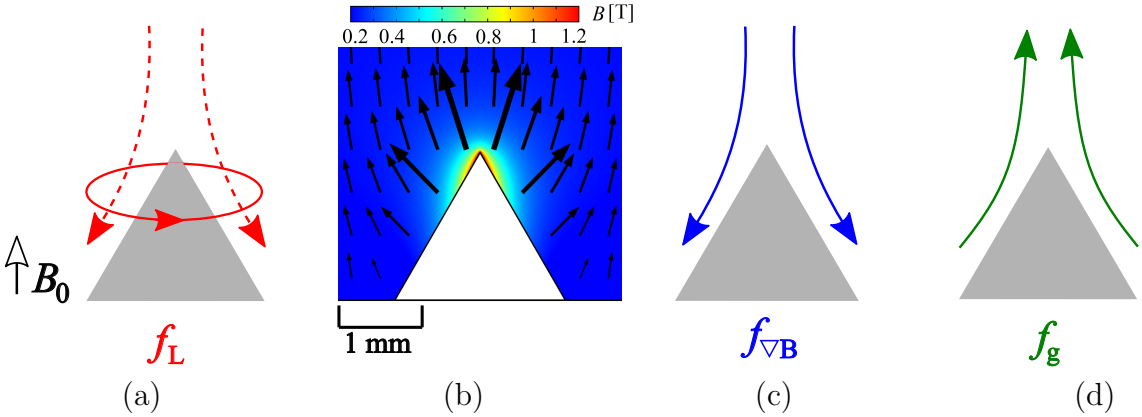

Figure 1: Sketch of the flows generated by (a) the Lorentz force $\boldsymbol{f}_{\mathbf{L}}$ (primary and secondary flow indicated by solid and dashed lines, respectively), (c) the magnetic gradient force $\boldsymbol{f}_{\boldsymbol{\nabla}\mathbf{B}}$ and (d) the buoyancy force $\boldsymbol{f}_{\mathbf{g}}$ near a conical cathode under the influence of an external vertical magnetic field B_0. (b) Vectors and color contours of the magnetic flux density $\boldsymbol{B}$ near a single Fe cone (diameter 2mm, tip angle 60°, $B_0 = 200$ mT; simulation result).

If the deposition is performed in an inhomogeneous magnetic field, the gradient of the magnetic field gives rise to a magnetic gradient force, which may also cause electrolyte flow and thus affect the deposition processes. If the length scale over which the magnetic field changes is small, e.g. below 1 mm, a strong field gradient is created, and the magnetic gradient force may even dominate over the Lorentz force [33]. In the case of the ferromagnetic layers studied here, the field gradient is caused by the magnetization of the cones distorting the uniform external magnetic field. Figure 1(b) shows the magnetic field distribution near a Fe cone in the vertical center plane when a uniform external vertical field of 200 mT is applied. Here, the magnetization of the Fe cone has not yet completely reached the saturation level [36], and large magnitudes of magnetic induction are visible near the tip, creating

strong field gradients. The magnetic gradient force is given as [33]:

$$\boldsymbol{f}_{\boldsymbol{\nabla}\mathbf{B}} = \chi_{\mathrm{sol}}/\mu_0(\boldsymbol{B}\cdot\nabla)\boldsymbol{B}, \qquad \chi_{\mathrm{sol}} = \sum_i \chi_i^{\mathrm{mol}} c_i + \chi_{\mathrm{H_2O}} \tag{2}$$

Here, $\mu_0 = 4\pi \cdot 10^{-7}\,\mathrm{Vs/(Am)}$, c_i, χ_i^{mol}, $\chi_{\mathrm{H_2O}}$ and χ_{sol} denote the vacuum permeability, the concentration and the molar magnetic susceptibility of species i, and the magnetic susceptibilities of water and the solution, respectively.

It has been pointed out previously that for electrodeposition performed in a closed electrochemical cell bounded by walls, the potential parts of forces are balanced by the wall pressure and cannot drive electrolyte flow [30]. Therefore, with respect to $\boldsymbol{f}_{\boldsymbol{\nabla}\mathbf{B}}$ studied here, the rotational part is responsible for the resulting flow [33]:

$$\nabla \times \boldsymbol{f}_{\boldsymbol{\nabla}\mathbf{B}} = \frac{1}{2\mu_0}(\sum_i \chi_i^{\mathrm{mol}} \nabla c_i) \times (\nabla B^2) \tag{3}$$

Thus, the flow forced by $\boldsymbol{f}_{\boldsymbol{\nabla}\mathbf{B}}$ is determined by the gradients of the species concentrations and of the magnetic field. As the concentration gradient near the cathode develops with ongoing deposition, the magnitude and direction of $\boldsymbol{f}_{\boldsymbol{\nabla}\mathbf{B}}$ will vary over time. Fig. 1 (c) shows a possible flow pattern caused by $\boldsymbol{f}_{\boldsymbol{\nabla}\mathbf{B}}$.

Beside the magnetic forces, the buoyancy force which arises from variations in the density of the electrolyte may also cause electrolyte flow during electrodeposition [37]:

$$\boldsymbol{f}_{\mathbf{g}} = (\rho - \rho_0)\boldsymbol{g} \tag{4}$$

Here, ρ, ρ_0 and $\boldsymbol{g} = -9.81\mathrm{m/s}^2\,\boldsymbol{e_z}$ denote the local and the bulk density of the electrolyte and the vector of the gravitational acceleration which points in a downward direction $-\boldsymbol{e_z}$ (see Fig. 2 for the coordinate system). Density variations originate from a spatially varying electrolyte composition caused by electrode reactions or from temperature variations in the electrolyte caused by Ohmic heating. However, the thermal effect is often much smaller than the solutal one and can be safely neglected, see Section 2.3.

In the following we consider electrochemical cells where the cathode is placed at the bottom. The metal deposition at the cathode reduces the density of the electrolyte, and solutal buoyancy tends to bring upward the lighter electrolyte, as shown in Fig. 1(d). As the cathodes considered are not planar in shape, even in the case of homogeneous deposition, $\boldsymbol{f}_{\mathbf{g}}$ has a non-zero rotational part, which drives a horizontal flow towards the foot of the cone and an upward flow along the cone surface:

$$\nabla \times \boldsymbol{f}_{\mathbf{g}} = g\nabla\rho \times \boldsymbol{e}_z \tag{5}$$

As the deposition starts, this flow sets in unconditionally, which is different from solutal convection at planar horizontal electrodes; this requires a critical Rayleigh number to start [38]. The upward flow along the cone can be expected to generate a

concentration boundary layer of growing thickness. Thus, near the cone tip, the concentration gradient and diffusive mass transfer may be weakened, and cone growth supported by only the geometrical non-uniformity of the cathode may be impeded. In this respect, properly adjusted magnetic fields offer the possibility to force an opposing flow that is strong enough to compensate for the unfavorable buoyancy flow and thus to enhance the desired structuring effect.

Extending the reflections to include planar cathodes with several conical elevations (see Fig. 2), the flow generated near each single cone may interact with flow originating from its neighbors. Corresponding damping of the azimuthal flow near magnetically templated electrodes was already reported in [39]. However, the neighbor influence on the magnetization, the resulting magnetic gradient force and also the impact of buoyancy has not been studied so far.

This work aims at studying the utilization of magnetic fields for the electrodeposition of conically structured ferromagnetic deposits. Although the majority of today's practical applications are for micro- and nano-sized conical structures, here we perform first investigations on a larger scale to gain a basic understanding of the magnetic field effects. This work extends the earlier study related to Lorentz force effects with single cones [1] and firstly elaborates on the magnetic gradient force, which plays an important role at ferromagnetic layers. The study includes single cones of different shapes and also the influence of neighboring cones at varying distances from one another. Thus, a detailed understanding is gained of the contributions made by the different forces involved during electrodeposition in a vertical magnetic field.

2. Methods

2.1. Problem description and simulation approach

We perform transient numerical simulations for the galvanostatic electrodeposition of metal on planar cathodes with periodic arrangements of conical elevations. The electrodes are oriented horizontally, and the electrochemical cell is exposed to a uniform magnetic field which is oriented vertically. We consider cathodes made of iron and additionally also of copper, to compare with earlier investigations at diamagnetic electrodes [1]. In order to study the basic effects of both magnetic forces, as well as the influence of neighbor effects, we start with cones of mm size, which will also facilitate the later experimental validation of our simulation results. The deposition times considered are in the range of minutes. We can therefore neglect changes of the electrode shape during deposition and treat the electrode geometry as fixed. Hence, the magnetic field near the electrodes also does not change during deposition. In order to further exclude any possible influence from the different reaction kinetics of the metals deposited, we deposit copper at both the ferromagnetic

and the diamagnetic cathodes. We also neglect any possible side reactions such as the hydrogen evolution reaction.

Our simulation approach consists of three steps which are outlined in Fig. 2. In the first step, we study the generic behavior at single cones and neglect any influence from neighboring cones, which are assumed to be far away. Thus, in a cylindrical region with the cone placed in the center of the cathode, the problem can be assumed to be axisymmetrical. The computational domain is thus the vertical plane bounded by the symmetry axis and the outer mantle boundary, and by the electrodes (see Fig. 2(a-b)). The simulations allow for an azimuthal flow caused by the Lorentz force, but neglect any dependencies on the azimuthal (θ) position.

In the second step, we take neighbor effects into account. We consider an infinitely extended planar cathode with a regular checkerboard arrangement of conical deformations (see Fig. 2(c-d)). In the following we assume that the electrodeposition proceeds identically at all cones. Global effects originating from e.g. recirculating flows around electrodes of finite size [28] are beyond the scope of this study. We therefore pick a cuboid computational domain between the electrodes where the cone is located in the center of the cathode square. The side length of the square corresponds to the cone distance, which will be varied later to study different cone densities. At the opposite vertical faces of the cuboid domain, periodic boundary conditions will be applied in the simulations.

As these simulations have to be performed in 3D and are expensive in terms of computing resources, in the third step, we introduce an approximate scheme for considering the neighbor influence. In order to facilitate simpler axisymmetric simulations, we assume that there are neighboring cones at the same distance for all azimuthal directions. Thus, the cylindrical domain shown in Fig. 2(a-b) can be used again. Here, in contrast to Step 1, the radial extension is defined as half the distance between the cones. At this outer domain boundary, for reasons of symmetry, the flow has no radial component, and the azimuthal component originating from the Lorentz force can be expected to be canceled out, as the azimuthal flow direction is opposite between neighbors. This approximation allows 2D simulations to be performed instead of 3D simulations as a means of considering the influence of neighboring cones, and will be validated below by presenting a comparison of the two simulation approaches for the case of the copper cones. The boundary conditions applied in the three steps will be explained in full detail in Section 2.2.

2.2. Model equations and boundary conditions

The numerical model consists of a coupled system of equations for the magnetic field, the electrolyte velocity, the concentration of the ionic species and the electric field. The computational domains for the three steps of the simulations are outlined in Fig. 2(b)(d), and the boundary conditions applied are summarized in Table 1.

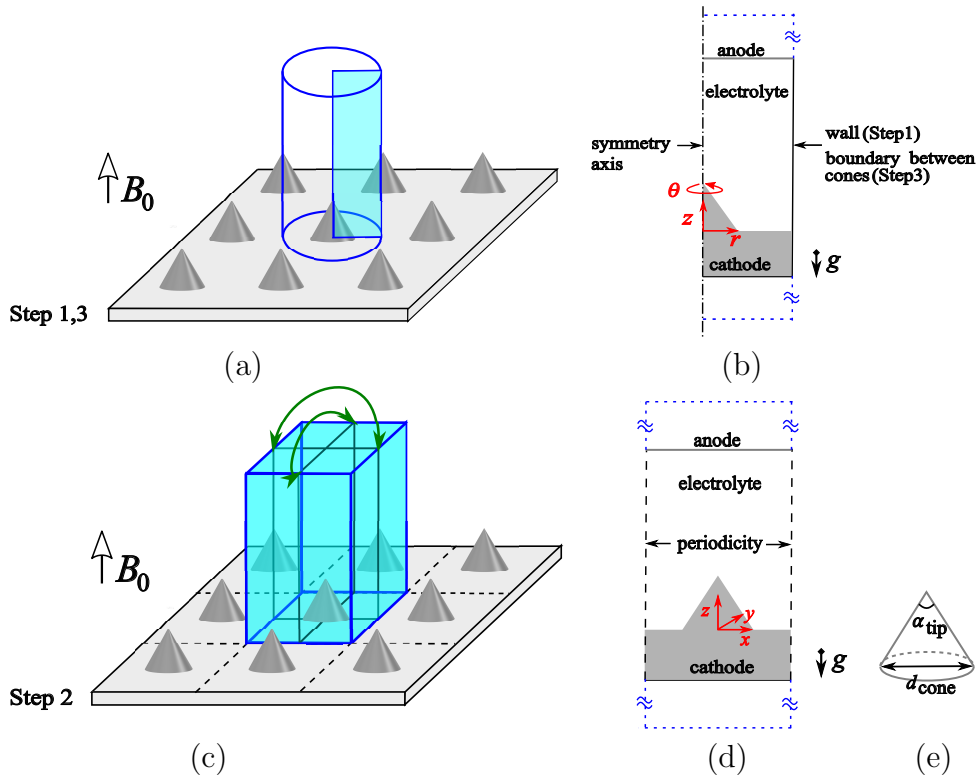

Figure 2: Sketch of the computational domains (marked in light blue), the related coordinate systems (cylindrical in (b) and Cartesian in (d)) and the specific boundary conditions applied to illustrate the three steps of the computational approach. (a-b) Step 1 and Step 3. (c-d) Step 2. At the opposite vertical faces of the cuboid, green arrows indicate the periodic boundary conditions which are applied. The dashed blue lines indicate the vertically extended domains for calculating the magnetic field. (e) Sketch of the cone geometry with α_{tip} and d_{cone} denoting the cone tip angle and the cone diameter. For more details see Sections 2.1 and 2.2.

The magnetic field is obtained by solving the Maxwell equations [40]:

$$\nabla \cdot \boldsymbol{B} = 0, \qquad \nabla \times \boldsymbol{H} = 0 \tag{6}$$

The magnetic field strength $\boldsymbol{H}$ is linearly related to the magnetic flux density $\boldsymbol{B}$ by the vacuum permeability μ_0 for the paramagnetic and diamagnetic materials in our calculations, i.e. $\boldsymbol{B} = \mu_0 \boldsymbol{H}$. Inside the ferromagnetic cathodes, there is

$$\boldsymbol{B} = \mu_0(\boldsymbol{H} + \boldsymbol{M}) \tag{7}$$

Here, the magnetization $\boldsymbol{M}$ is given by a corresponding magnetization curve [41]. $\boldsymbol{H}$ is the sum of the external field strength $(\boldsymbol{B_0}/\mu_0)$ and the demagnetizing field, the latter being directed antiparallel to $\boldsymbol{M}$ in ferromagnetic materials [42]. We apply $\boldsymbol{B} = \boldsymbol{B_0}$ on the outer horizontal boundaries of the magnetic field domain for all three steps and at the vertical side wall of Step 1, because a homogeneous external magnetic field is imposed on the cell. For Steps 2 and 3, the neighboring effects imply symmetry conditions at the vertical boundaries between the cones. We therefore apply periodic conditions at the oppositely located vertical boundaries of the cuboid domain in Step 2, and $\boldsymbol{B} \cdot \boldsymbol{n} = 0$ at the outer radius in Step 3. Here $\boldsymbol{n}$

denotes the unit vector normal to the boundary. It should be mentioned that the magnetic boundary conditions applied here exclude specific deposition effects at the outer edges of the planar part of the ferromagnetic electrode found elsewhere [16].

The electrolyte velocity $\boldsymbol{U}$ is obtained by solving the Navier-Stokes equations including the volume forces mentioned above and complemented by the incompressibility constraint,

$$\rho_0 \left(\frac{\partial \boldsymbol{U}}{\partial t} + (\boldsymbol{U} \cdot \nabla)\boldsymbol{U} \right) = -\nabla P + \mu \nabla^2 \boldsymbol{U} + \boldsymbol{f}_{\mathbf{L}} + \boldsymbol{f}_{\nabla \mathbf{B}} + \boldsymbol{f}_{\mathbf{g}}, \qquad \nabla \cdot \boldsymbol{U} = 0 \tag{8}$$

Here, P and μ denote the dynamic pressure and the dynamic viscosity of the electrolyte. A no-slip boundary condition is applied at the electrodes for all steps and at the vertical side wall for Step 1. For Step 2, periodic boundary conditions are enforced at the vertical boundaries. For Step 3, symmetry with respect to the neighbor influence allows a free-slip boundary condition to be applied ($\boldsymbol{U} \cdot \boldsymbol{n} = 0$) at the outer radius, supplemented by the constraint that the azimuthal velocity (U_θ) has to vanish.

The distribution of species in the electrolyte is obtained by solving the Nernst-Planck equations of dilute solutions:

$$\frac{\partial c_i}{\partial t} = -\nabla \boldsymbol{\cdot} \boldsymbol{N_i} \tag{9}$$

Here, $\boldsymbol{N_i}$ denotes the flux density of species i

$$\boldsymbol{N_i} = -z_i F \frac{D_i}{RT} c_i \nabla \phi - D_i \nabla c_i + c_i \boldsymbol{U} \tag{10}$$

which, beside transport by migration and diffusion, also includes convective transport by the electrolyte velocity from Eq. (8) [37]. Here, z_i, D_i, F, R, T and ϕ are the charge number and the diffusion coefficient of species i, the Faraday constant, the universal gas constant, the temperature and the electric potential, respectively. The electric current density in the solution is the net flux density of all charged species:

$$\boldsymbol{j} = F \sum_i z_i \boldsymbol{N_i} \tag{11}$$

We further assume electroneutrality in the electrolyte, i.e. $\sum z_i c_i = 0$. Combining Eqs. 10, 11 and the conservation of charge ($\nabla \cdot \boldsymbol{j} = 0$), the electric potential can be obtained as the solution of a Poisson equation:

$$\nabla \cdot \left(-F^2 \nabla \phi \sum_i z_i^2 \frac{D_i c_i}{RT} \right) - \nabla \cdot \left(F \sum_i z_i D_i \nabla c_i \right) = 0 \tag{12}$$

Regarding the boundary conditions applied, on electrically passive walls, due to electric insulation, the normal components of the electric current and the flux of all

ionic species have to vanish for Step 1. The same boundary conditions are applied for Step 3, but for reasons of symmetry. For Step 2, periodic boundary conditions are again implemented. On the electrodes, a Butler-Volmer relation is applied to describe the kinetics of the copper reaction for all three steps [37]:

$$j_n = j_0 \left(exp\left(\frac{\alpha_\mathrm{a} F \eta_\mathrm{s}}{RT}\right) - exp\left(\frac{-\alpha_\mathrm{c} F \eta_\mathrm{s}}{RT}\right)\right) \tag{13}$$

Here j_0, α_a and α_c denote the exchange current density and the apparent transfer coefficients. The surface overpotential η_s is defined as the potential of the electrode ϕ_e relative to the solution potential ϕ minus the equilibrium electrode potential ϕ_eq given by the Nernst equation, i.e. $\eta_\mathrm{s} = \phi_\mathrm{e} - \phi - \phi_\mathrm{eq}$ [37]. In the simulations, the electrode potential is adjusted at each time step to satisfy the galvanostatic condition $I = I(\phi_\mathrm{e}) = const.$

Table 1: Boundary conditions applied in the different steps of the simulations. The subsripts "src" and "dst" denote the source and the destination boundaries in the case of periodic boundary conditions (see Fig. 2 (c-d)).

	Boundary	Step 1	Step 2	Step 3
Magnetic field	Axis	$\partial \boldsymbol{B}/\partial r = 0$	-	$\partial \boldsymbol{B}/\partial r = 0$
	Vertical	$\boldsymbol{B} = \boldsymbol{B_0}$	$\boldsymbol{B_{\mathrm{src}}} = \boldsymbol{B_{\mathrm{dst}}}$	$\boldsymbol{B} \cdot \boldsymbol{n} = \boldsymbol{0}$
	Horizontal	$\boldsymbol{B} = \boldsymbol{B_0}$		
Electrolyte velocity	Axis	$\partial \boldsymbol{U}/\partial r = 0$	-	$\partial \boldsymbol{U}/\partial r = 0$
	Vertical	$\boldsymbol{U} = \boldsymbol{0}$	$\boldsymbol{U_{\mathrm{src}}} = \boldsymbol{U_{\mathrm{dst}}}$	$\boldsymbol{U} \cdot \boldsymbol{n} = \boldsymbol{0}, U_\theta = 0$
	Electrodes	$\boldsymbol{U} = \boldsymbol{0}$		
Electric field	Axis	$\partial \boldsymbol{j}/\partial r = 0$	-	$\partial \boldsymbol{j}/\partial r = 0$
	Vertical	$\boldsymbol{j} \cdot \boldsymbol{n} = \boldsymbol{0}$	$\boldsymbol{j_{\mathrm{src}}} = \boldsymbol{j_{\mathrm{dst}}}$	$\boldsymbol{j} \cdot \boldsymbol{n} = \boldsymbol{0}$
	Electrodes	$\boldsymbol{j} \cdot \boldsymbol{n}$ from Eq. 13		
Species	Axis	$\partial \boldsymbol{N}_i/\partial r = 0$	-	$\partial \boldsymbol{N}_i/\partial r = 0$
	Vertical	$\boldsymbol{N_i} \cdot \boldsymbol{n} = \boldsymbol{0}$	$\boldsymbol{N_{\mathrm{i,src}}} = \boldsymbol{N_{\mathrm{i,dst}}}$	$\boldsymbol{N_i} \cdot \boldsymbol{n} = \boldsymbol{0}$
	Electrodes	Passive ions: $\boldsymbol{N_i} = \boldsymbol{0}$		
		Active ions: $\boldsymbol{N_i} \cdot \boldsymbol{n}$ from Eq. 11, Eq. 13		

2.3. Material and simulation parameters

The material parameters for solving Eqs. 8-13 are listed in Table 2. The electrolyte is an aqueous 0.1 M $CuSO_4$ solution at room temperature. Because of electrical neutrality, it holds that $c_{\mathrm{Cu^{2+}}} = c_{\mathrm{SO_4^{2-}}}$, and the species index i can be omitted in the following. With respect to the reaction kinetics of copper, the exchange current density j_0 is given as $j_0 = j_{00}\,(c_\mathrm{s}/c_0)^\gamma$, with c_s and c_0 denoting the surface and the bulk concentration of the electroactive Cu^{2+} species. The reference exchange current density j_{00} and the kinetic parameter γ are taken from [43]. In the simulations performed, we found that the influence of the concentration-related term of the Nernst equation on the surface overpotential is negligibly small. We therefore take ϕ_eq to be equal to the standard equilibrium potential, $\phi_{\mathrm{eq},0}$, which reduces the non-linearity of the boundary condition.

The simulation parameters are summarized in Table 3. For the single cone studies of Step 1, a cone is considered with a base diameter of $d_{\text{cone}} = 2$ mm and a tip angle of $\alpha_{\text{tip}} = 60°$. These dimensions are varied only in the cone shape studies, see Section 3.2. The chosen cell height of 30 mm is large enough to avoid any influence from the anodic mass transfer at the cathode. The radial extension of the electrochemical cell is chosen to be 5 d_{cone}, which is large enough to ensure that the flow forced near the cone is not affected by the side wall. The current density used for the simulations in the three steps varies between 8 and 16 mA/cm^2. In order to obtain comparable amplitudes of the Lorentz force, the magnetic field amplitude is accordingly adjusted between 200 and 400 mT.

We now come back to estimating the relative significance of thermal and solutal buoyancy. For the maximum current density considered, of 16 mA/cm^2, when the Joule heat is assumed to be completely transferred to the electrolyte, the local temperature rises by about 0.2 K within one minute. The corresponding thermal density variation is less than 0.01% [44, 45]. However, assuming there is a concentration variation of 0.1 M, the solutal density variation is more than 100 times larger and reaches about 1.6% [45, 46]. Thermal buoyancy can therefore safely be neglected in the following. As the solutal density variation is still small, we may apply the Boussinesq approximation [38], and the buoyancy force expressed by Eq. 4 can be simplified to:

$$\boldsymbol{f}_{\mathbf{g}} = \rho_0 \boldsymbol{g} \beta_{\text{CuSO}_4} (c - c_0) \tag{14}$$

with β_{CuSO_4} denoting the volume expansion coefficient of the electrolyte (Table 2).

Table 2: Material parameters for 0.1 M $CuSO_4$ at room temperature.

$\chi^{\text{mol}}_{\text{Cu}^{2+}}$ (m^3/mol)	$1.57 \cdot 10^{-8}$	[32]
$\chi_{\text{H}_2\text{O}}$	$-9.0 \cdot 10^{-6}$	
ρ_0 (kg/m^3)	1014	[46]
β_{CuSO_4} (m^3/mol)	$1.6 \cdot 10^{-4}$	
μ (Pa $\cdot$ s)	$1.04 \cdot 10^{-3}$	
$D_{\text{Cu}^{2+}}$ (m^2/s)	$5.6 \cdot 10^{-10}$	[43]
$D_{\text{SO}_4^{2-}}$ (m^2/s)	$10.04 \cdot 10^{-10}$	
$z_{\text{Cu}^{2+}}$	2	
$z_{\text{SO}_4^{2-}}$	-2	
j_{00} (mA/cm^2)	10	[37, 43]
$\phi_{\text{eq},0}$ (V)	0.337	
γ	0.42	
α_{a}	1.5	
α_{c}	0.5	

2.4. Numerical details and validations

The simulations were performed using the Finite Element software package Comsol V.5.5 [41]. Second-order shape functions are used for the magnetic field $\boldsymbol{B}$, the

Table 3: Simulation parameters.

	Step 1			Step 2	Step 3
α_{tip}	30°	60°	90°	60°	60°
d_{cone} (mm)	1.4	2	2.4	2	2
Cone surface area (mm^2)	6.28			6.28	6.28
Cell height (mm)	30			30	30
Height of magnetic field domain (mm)	100			100	100
Cell width (mm)	10			-	-
Cone distance (d_{cone})	-			$1.5, 2, 3, 5$	$1.5, 2, 3, 5$
$j_{\text{cathode,avg}}$ (mA/cm^2)	16			8	8
B_0 (mT)	200			400	400
c_0 (M)	0.1			0.1	0.1

velocity $\boldsymbol{U}$, the concentration c and the electric potential ϕ, and first-order shape functions are used for the pressure P. The initial conditions for the transient simulations are an electrolyte with a homogeneous bulk concentration c_0 at rest, i.e. $\boldsymbol{U} = 0$. Time integration was carried out using an implicit backward differentiation formula method of up to the second order. The time step is adjusted by the solver based on error estimation during the calculations, with an upper limit of 0.1 s which, according to a time-step study, ensures the accuracy of the results.

Unstructured triangular (2D) or prismatic (3D) meshes were generated and refined near the boundaries so as to sufficiently resolve the spatial gradients of the concentration, the velocity and the magnetic field. A mesh study has shown that the steep magnetic field gradients near the Fe cones are most demanding. Thus, the mesh size near the cone surface was chosen to be $0.0005\, d_{\text{cone}}$ for the Fe cones and $0.001\, d_{\text{cone}}$ for the Cu cones, respectively. This choice also ensures the sufficient resolution of the concentration and velocity boundary layers.

For the magnetic field, a domain size study was performed to ensure that the proximity of the top and bottom boundary does not affect the field distribution inside the electrochemical cell. The magnetic field distributions obtained numerically have further been validated with experimental data for different magnet geometries [1]. As a result, a domain height of 100 mm was chosen.

The full numerical model described above was validated by experimental data from a similar deposition process on a single Cu cone [1] and also by deposition problems at magnetically templated electrodes, where the magnetic gradient force is of importance [33, 34]. As a result, the numerical model is able to deliver accurate, reliable information on the magnetic field distribution, the electrolyte flow, the species distribution and the current density distribution in the cell.

3. Results and Discussion

3.1. Single cones

In the following, the generic case of single cones (Step 1) is considered in order to obtain a basic understanding of the influence of the different volume forces involved in the deposition process. An intermediate tip angle of 60° is chosen for the copper and iron cones investigated. Fig. 3 shows the azimuthal flow driven by the Lorentz force $\boldsymbol{f}_\mathbf{L}$ after a deposition time of 10 s. Surprisingly, an opposite direction of rotation is observed for the iron cone compared to the copper cone. Moreover, the azimuthal flow for the iron cone extends over a smaller area than for the copper cone. This can be understood by considering the Lorentz force of the axisymmetric problem, which consists of an azimuthal component only:

$$\boldsymbol{f}_\mathbf{L} = (j_\mathrm{z} B_\mathrm{r} - j_\mathrm{r} B_\mathrm{z})\boldsymbol{e}_{\boldsymbol{\theta}} \tag{15}$$

Here, $\boldsymbol{e}_{\boldsymbol{\theta}}$ denotes the unity vector in the azimuthal direction (Fig. 2(b)). In general, when approaching the cone, the vertical current density vectors bend towards the surface-normal direction of the cone. Thus, $j_\mathrm{r} < 0$, $j_\mathrm{z} < 0$. For the Cu case, the magnetic field is not modified by the diamagnetic cathode, and the magnetic field equals the external vertical field applied, i.e. $B_\mathrm{r} = 0, B_\mathrm{z} = B_0$. Therefore, as shown on the right-hand side of Fig. 3, $j_r B_0 < 0$ is responsible for the anticlockwise rotation seen from the top of the cell.

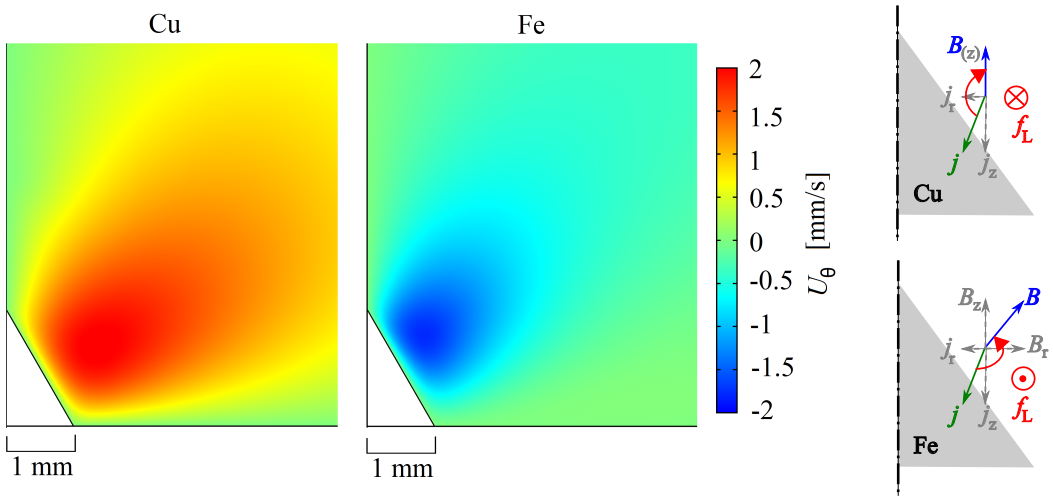

Figure 3: Color surface of the azimuthal velocity after 10 s deposition time near the Cu and the Fe cones ($\alpha_\mathrm{tip} = 60°$, $j_\mathrm{cathode,avg} = 16$ mA/cm^2, $B_0 = 200$ mT). The direction of azimuthal forcing by the Lorentz force is outlined on the far right.

For the Fe case, the magnetic field is modified in the vicinity of the cone due to its magnetization, as shown in Fig. 1. Unlike the Cu case, radial components of $\boldsymbol{B}$ give rise to negative force amplitudes $j_\mathrm{z} B_\mathrm{r}$ which may exceed the positive part $(-j_\mathrm{r} B_\mathrm{z})$. The resulting clockwise forcing is shown on the right-hand side of Fig. 3. As large radial components of the magnetic field are only found close to the surface of the

magnetized cone, the region of rotation is smaller compared to the Cu case. Similar clockwise rotation was also found for the steeper and flatter iron cones investigated in Section 3.2. However, it should be noted that, irrespective of the direction of the azimuthal flow, the secondary flow created by the centrifugal force is always directed downwards towards the cone tip [33, 39].

Fig. 4 compares the meridional velocity near the Cu and Fe cones with and without a magnetic field after 5 s and 10 s of deposition time. In the absence of the magnetic field, the behavior is identical for Cu and Fe cones. An upward-directed buoyant flow develops with ongoing deposition, reaching a velocity of about 1 mm/s above the cone after 10 s of deposition. Similar flow pattern were found in an earlier study of copper deposition at a copper cone in a weak vertical magnetic field of 60 mT. There, the downward acceleration generated by the Lorentz force was not strong enough to reverse the direction of flow, and the concentration boundary layer was advected upwards and detached at the cone tip [1]. In the following, a stronger

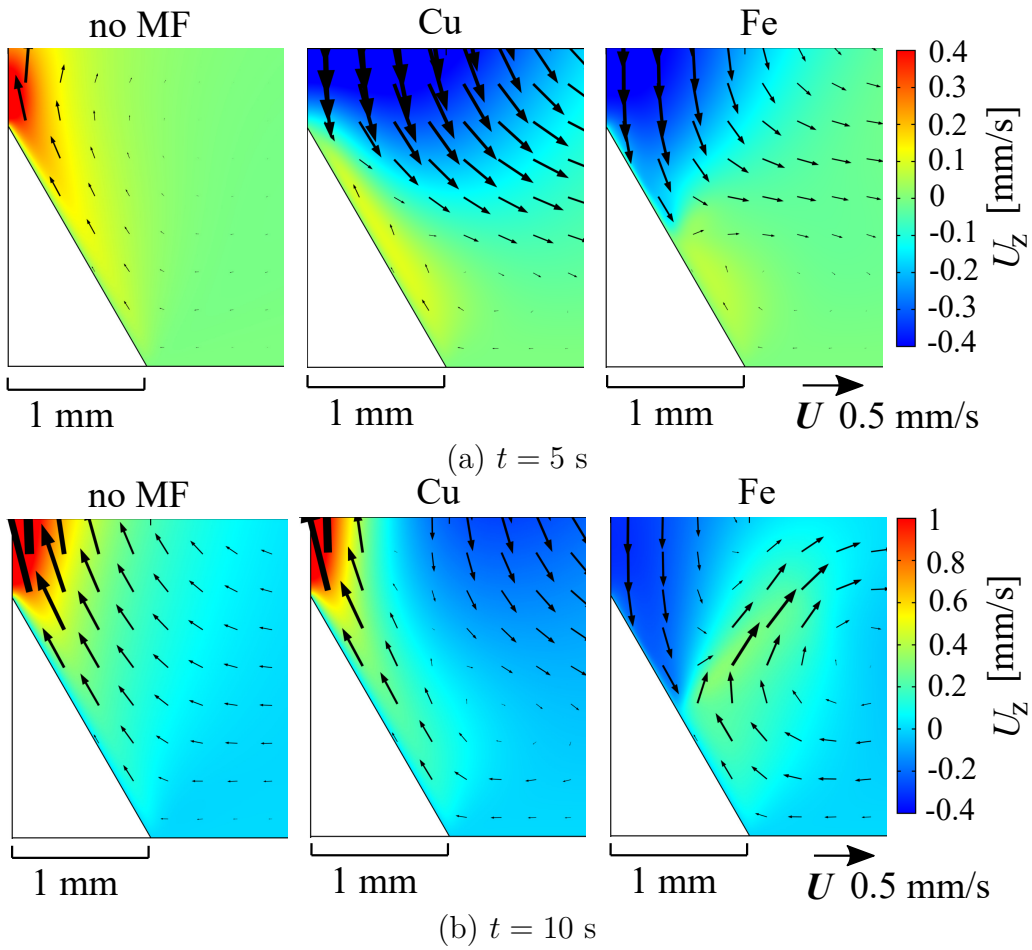

Figure 4: Color surface of the vertical velocity after 5 s and 10 s deposition time near a cone without a magnetic field (left: no MF), near the Cu cone with a magnetic field (middle) and the Fe cone with a magnetic field (right). $\alpha_{\text{tip}} = 60^\circ$, $j_{\text{cathode,avg}} = 16$ mA/cm^2, $B_0 = 200$ mT. Black arrows represent the meridional velocity vectors.

magnetic field of 200 mT is considered. As shown in Fig. 4, near the copper cone after a deposition time of 5 s a strong downward-directed flow is clearly visible, which can be attributed to the dominant secondary flow caused by the Lorentz

force. However, the flow direction very close to the cone surface has already turned upwards due to the buoyancy of the concentration boundary layer, indicated by the yellow region. As the deposition continues, the buoyant flow accelerates with time. As shown after 10 s, the direction of flow near the surface of the cone is dominated by buoyancy, which causes the concentration boundary layer to detach from the tip of the cone. A weak downward flow remains at a larger distance from the cone.

For the Fe cone in the magnetic field, the magnetic gradient force $\boldsymbol{f}_{\boldsymbol{\nabla}\mathbf{B}}$ also comes into play. In comparison to the copper case, the downward flow close to the cone surface seems to be stronger. After 5 s, the downward flow along the upper cone region is clearly visible, whereas the flow velocity near the lower part of the cone is low. After 10 s of deposition, the downward flow along the upper cone region is still maintained, but an upward flow caused by buoyancy is clearly visible in the lower part. This results in a jet-like flow leaving the cone surface in an approximately normal direction at about half the height of the cone. Although the influence of $\boldsymbol{f}_{\mathbf{L}}$ in the case of the iron cone is slightly weaker than in the case of the copper cone, $\boldsymbol{f}_{\boldsymbol{\nabla}\mathbf{B}}$ is effectively counteracting $\boldsymbol{f}_{\mathbf{g}}$ in the vicinity of the cone surface.

In order to further analyze the influence of $\boldsymbol{f}_{\boldsymbol{\nabla}\mathbf{B}}$ on the deposition process, Figs. 5(a-b) show the concentration of the copper ions close to the iron cone after a deposition time of 5 s and 10 s. The images are superimposed with the meridional velocity vectors. The downward flow along the surface of the upper part of the cone continuously brings fresh bulk electrolyte to the tip, keeping the local concentration boundary layer thin. By contrast, the upward buoyant flow already originates at the horizontal part of the cathode, with a horizontal flow towards the cone, and the thickness of the concentration boundary layer there grows with time. The aforementioned jet-like flow about halfway up the cone is accompanied by the corresponding detachment and advection of the concentration boundary layer in an approximately electrode-normal direction. A similar effect of boundary layer separation caused by the opposing action of $\boldsymbol{f}_{\mathbf{L}}$ and $\boldsymbol{f}_{\mathbf{g}}$ during electrodeposition was already reported elsewhere [47].

The concentration boundary layer near the cone, in turn, affects $\boldsymbol{f}_{\boldsymbol{\nabla}\mathbf{B}}$ and thus the flow field. Applying Eq. 2, based on the material parameters given in Table 2, the magnetic susceptibility of the bulk solution is negative, as the diamagnetic contribution of the water molecules dominates [32]:

$$\chi_{\mathrm{sol}} = \chi^{\mathrm{mol}}_{\mathrm{Cu^{2+}}} c_0 + \chi_{\mathrm{H_2O}} = -7.43 \cdot 10^{-6} \tag{16}$$

This also holds inside the concentration boundary layer, where $c_{\mathrm{Cu^{2+}}} \leq c_0$ can be assumed. Therefore, $\boldsymbol{f}_{\boldsymbol{\nabla}\mathbf{B}}$ is acting in the opposite direction to that of the magnetic gradient. As the strongest magnetic field is found near the tip of the cone, $\boldsymbol{f}_{\boldsymbol{\nabla}\mathbf{B}}$ points away from the tip. However, this contradicts the simulation result, which indicates that the electrolyte flow is directed towards the tip. This issue can easily

be resolved by only considering the rotational parts of the magnetic gradient force and the buoyancy force, as discussed in the introduction. As axisymmetry applies, the curl of both forces defined in Eqs. 3 and 5 in cylindrical coordinates reads:

$$\nabla \times \boldsymbol{f}_{\boldsymbol{\nabla}\mathbf{B}} = \frac{\chi^{\mathrm{mol}}}{\mu_0} \left(\frac{\partial c}{\partial z} B \frac{\partial B}{\partial r} - \frac{\partial c}{\partial r} B \frac{\partial B}{\partial z} \right) \boldsymbol{e}_{\boldsymbol{\theta}} \tag{17}$$

$$\nabla \times \boldsymbol{f}_{\mathbf{g}} = \beta_{\mathrm{c}} g \rho_0 \left(\frac{\partial c}{\partial r} \right) \boldsymbol{e}_{\boldsymbol{\theta}} \tag{18}$$

Near the cone surface, the concentration gradient vector essentially points away from the surface into the electrolyte volume, i.e. $\frac{\partial c}{\partial r} > 0, \frac{\partial c}{\partial z} > 0$ (see Fig. 5(b)). As the maximal magnetic field exists near the cone tip, along the cone surface $\frac{\partial B}{\partial r} < 0, \frac{\partial B}{\partial z} > 0$. According to Eq. 17, the resulting $\nabla \times \boldsymbol{f}_{\boldsymbol{\nabla}\mathbf{B}}$ has a negative azimuthal amplitude and forces the flow to rotate in an anticlockwise direction in the meridional plane, i.e. downwards along the cone surface. In contrast, $\nabla \times \boldsymbol{f}_{\mathbf{g}}$ has a positive azimuthal amplitude along the cone surface because $\frac{\partial c}{\partial r} > 0$. As the final flow is determined by the curl of both forces, in Fig. 5(c) the sum of $\nabla \times \boldsymbol{f}_{\boldsymbol{\nabla}\mathbf{B}}$ and $\nabla \times \boldsymbol{f}_{\mathbf{g}}$ is shown after 10 s of deposition time. It can be clearly seen that the upper part of the cone boundary layer is dominated by the negative curl of $\boldsymbol{f}_{\boldsymbol{\nabla}\mathbf{B}}$, whereas the lower part is dominated by the positive curl of $\boldsymbol{f}_{\mathbf{g}}$. This means that a downward flow is forced along the surface of the upper cone part, counteracting the upward buoyant flow. These flows force the jet-like departure of the concentration boundary layer from the cone surface at about mid-height. Thus, the azimuthal components of $\nabla \times \boldsymbol{f}_{\boldsymbol{\nabla}\mathbf{B}}$ and $\nabla \times \boldsymbol{f}_{\mathbf{g}}$ deliver a vivid interpretation of the flow pattern observed.

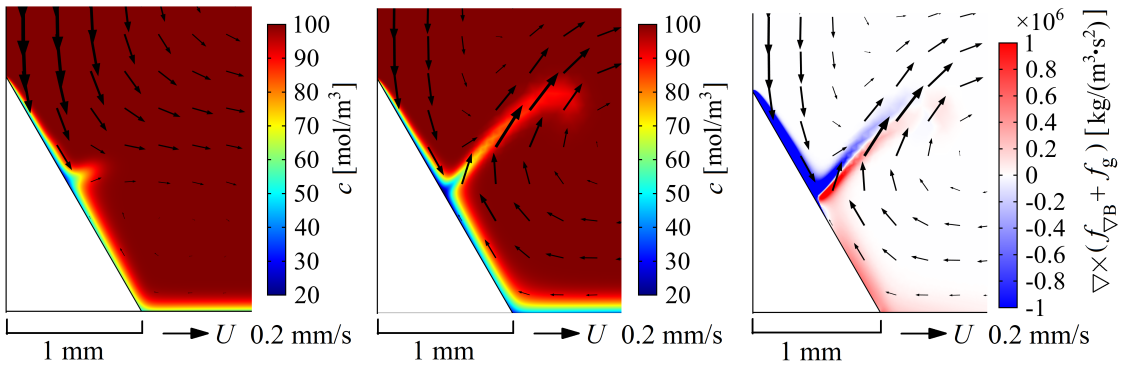

(a) c at 5 s (b) c at 10 s (c) $\nabla \times (\boldsymbol{f}_{\boldsymbol{\nabla}\mathbf{B}} + \boldsymbol{f}_{\mathbf{g}})$ at 10 s

Figure 5: Color surface of the concentration after (a) 5 s and (b) 10 s deposition time and (c) the sum of the curl of the magnetic gradient force and the buoyancy force after 10 s deposition near the Fe cone ($\alpha_{\mathrm{tip}} = 60^{\circ}$, $j_{\mathrm{cathode,avg}} = 16$ mA/cm^2, $B_0 = 200$ mT). Black arrows represent meridional velocity vectors.

The influence of the magnetic forces on the growth dynamics of conical elevations on the cathode can be evaluated by considering the deposit thickness along the cone surface [37]:

$$d(r,T) = \frac{V_{\mathrm{m}}}{zF} \int_0^T j_{\mathrm{n}}(r,t)dt \tag{19}$$

Here, $V_{\mathrm{m}} = 7.11 \times 10^{-6}$ m^3/mol denotes the molar volume of copper [48], and T denotes the deposition time. Fig. 6 shows the initial height contour of the cone (left) and the deposit thickness along the surface of the Cu and Fe cones after 10 s of deposition time (right). In the case without a magnetic field, the deposit thickness increases monotonically from the foot to the tip of the cone, as a result of the previously mentioned support for cone growth for geometrical reasons. Despite the counteraction of the upward buoyant flow discussed above, in total, cone growth would be supported.

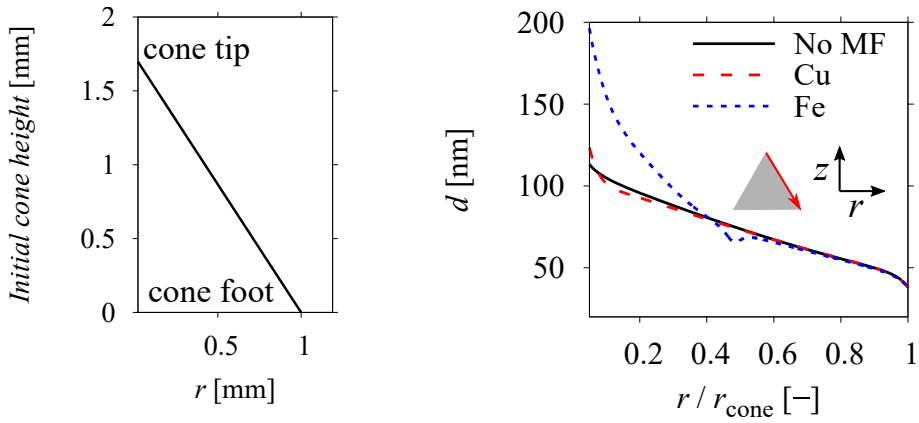

Figure 6: Left: Initial height contour of the cone. Right: Deposit thickness along the cone surface for the cases without magnetic field (No MF) and for Cu and Fe cones in a vertical magnetic field after 10 s deposition time ($\alpha_{\mathrm{tip}} = 60^\circ$, $j_{\mathrm{cathode,avg}} = 16$ mA/cm^2, $B_0 = 200$ mT). The horizontal axis is the radial surface coordinate normalized by the cone radius r_{cone}.

In the case of the copper cone in the vertical magnetic field, small differences are found with respect to the case without a magnetic field. Close to the tip of the cone, the thickness of the deposit is increased. This is a result of the downward secondary flow caused by $\boldsymbol{f}_{\mathbf{L}}$, which initially supersedes the upward buoyant flow. This reversal of the flow direction in the tip region in the first few seconds of the deposition enriches the boundary layer and thus enhances mass transfer, see Fig. S1 in the Supplementary Information (SI). In the region below, down to about half the height of the cone, the deposit is slightly thinner in comparison to the case without a magnetic field. This suggests that during the deposition period of 10 s, the counteraction between the opposing secondary flow and the buoyant flow may have briefly led to a thicker boundary layer in the region slightly below the cone tip. For a more detailed discussion we refer to section 3.2 and also to Fig. S1 in SI.

For the case of the iron cone in the magnetic field, stronger support for cone growth is found compared to the case of copper. As can be seen in Fig. 6, the deposit thickness in the upper half of the cone is considerably increased and almost doubled at the tip compared to the case without a magnetic field. This results from a stronger downward flow caused by the additional action of the magnetic gradient force $\boldsymbol{f}_{\boldsymbol{\nabla}\mathbf{B}}$ compared to the case of copper. The local minimum of the deposit thickness found at about $r/r_{cone} = 0.5$ is related to the detachment of the

concentration boundary layer in a jet-like flow, as shown in Fig. 5(b).

As a means of further assessing the impact of the different volume forces on the deposition process, the ratios of the magnetic forces to the buoyancy force are introduced as follows [33]:

$$R_{\mathrm{MHD}} = \frac{\int_{\mathrm{V}} \mid \boldsymbol{f}_{\mathbf{L}} \mid dV}{\int_{\mathrm{V}} \mid \boldsymbol{f}_{\mathbf{g}} \mid dV}, \qquad R_{\nabla\mathrm{B}} = \frac{\int_{\mathrm{V}} \mid \boldsymbol{f}_{\boldsymbol{\nabla}\mathbf{B}} \mid dV}{\int_{\mathrm{V}} \mid \boldsymbol{f}_{\mathbf{g}} \mid dV} \tag{20}$$

Here, the integration over volume V is restricted to the main flow region ($0 < r < 2.5\, d_{\mathrm{cone}}, 0 < z < 2.5\, d_{\mathrm{cone}}, 0 < \theta < 2\pi$). The temporal behavior of both quantities during the deposition process in the magnetic field is presented in Fig. 7.

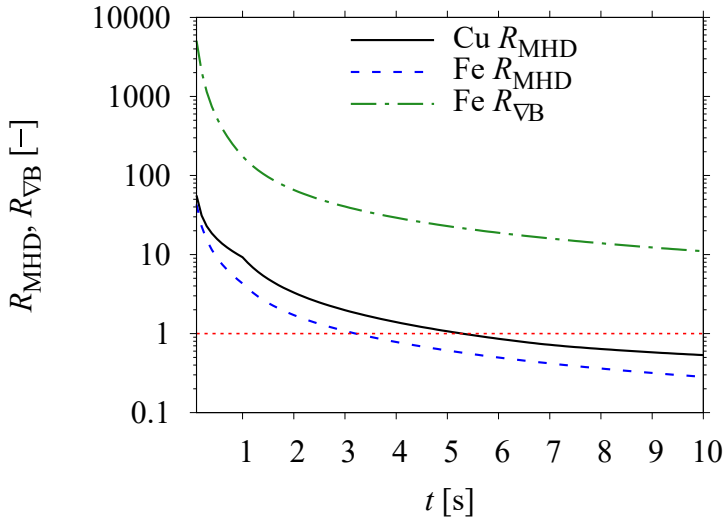

Figure 7: Temporal evolution of the force ratios R_{MHD} and $R_{\nabla\mathrm{B}}$ defined in Eq. (20) for deposition on single copper and iron cones ($\alpha_{\mathrm{tip}} = 60^{\circ}$, $j_{\mathrm{cathode,avg}} = 16$ mA/cm^2, $B_0 = 200$ mT). The vertical axis is shown on a logarithmic scale for better visibility, the red dashed line indicates the critical value of the force ratio of 1.

For both copper and iron cones, R_{MHD} shows a strong decrease with time. This is caused by the different temporal behavior of $\boldsymbol{f}_{\mathbf{L}}$ and $\boldsymbol{f}_{\mathbf{g}}$. As a galvanostatic process is considered, the current density distribution can be expected to change only slowly with ongoing deposition [1]. Therefore, $\boldsymbol{f}_{\mathbf{L}}$ is nearly constant, whereas $\boldsymbol{f}_{\mathbf{g}}$ grows considerably with time due to the development of the concentration boundary layer. In the case of copper, R_{MHD} sinks below the critical value of unity at $t \approx 5$ s. This is in line with the above discussion of the corresponding electrolyte flow pattern in Fig. 4. In comparison, in the case of iron R_{MHD} is slightly lower and already drops below unity at $t \approx 3$ s. This is in accordance with the primary flow shown in Fig. 3, which is only forced in a comparably smaller region, and therefore also results in a correspondingly weaker secondary flow.

The ratio of the magnetic gradient force to the buoyancy force $R_{\nabla\mathrm{B}}$ for the iron cone also shrinks with the deposition time. However, the values are much larger than in the two cases considered before. At the final instant considered, $t = 10$ s, $R_{\mathrm{MHD}} \approx 10$. This indicates that $\boldsymbol{f}_{\boldsymbol{\nabla}\mathbf{B}}$ has a much stronger influence on the process

than $\boldsymbol{f}_{\mathbf{L}}$ and also effectively counteracts the influence of $\boldsymbol{f}_{\mathbf{g}}$, which is in line with the discussion of the flow pattern shown in Fig. 4. It should be noted that the region where $\boldsymbol{f}_{\mathbf{g}}$ acts is extended with the buildup and the advection of the concentration boundary layer, while $\boldsymbol{f}_{\boldsymbol{\nabla}\mathbf{B}}$ is only of importance close to the cone where large field gradients are found. This easily explains the decrease in $R_{\nabla\mathrm{B}}$ with the deposition time.

3.2. Flat and sharp cones

To enable conclusions to be drawn on how a vertical magnetic field affects the growth of surface elevations at the different stages of development, we now include flat and steep cones in the investigation. The cone tip angles additionally considered are 30° and 90°, with the surface area of the cones remaining constant. More details of the cone dimensions are given in Table 3.

The shape of the cone can be expected to influence the distribution of the current density near the cone and also the magnetic field near the iron cone. We first investigate the influence of the current density. For geometrical reasons, steep cones are expected to be characterized by a less uniform current density distribution along the cone surface compared to flat cones [12]. This is also confirmed by the analytical solution of the primary current density distribution along an infinitely extended cone as derived in SI. Fig. 8(a) compares the numerically obtained primary current density distribution along the surface of the cones with different tip angles studied here, exhibiting good qualitative agreement with the analytical solution, as shown in Fig. S3 in SI.

In order to additionally account for kinetic effects at the electrode, which might mitigate the purely geometric effect considered in the primary current density [49, 50], Fig. 8(b) shows the numerical results of the current density at cones with different tip angles at $t = 10$ s. In these calculations, the electrode kinetics according to Eq. 13 are included, but the electrolyte flow is excluded. Although the inhomogeneity in general is reduced compared to the primary current density shown in Fig. 8(a), the numerical results indicate that the steep cone still has the largest value for the current density near the tip of the cone. This indicates a stronger Lorentz force effect for steeper cones.

A variation in the shape of the iron cones also affects the distribution of the magnetic field nearby. Fig. 9 shows the magnitudes of B and $B\nabla B$ along a nearby surface-parallel line for cones of different tip angles. In the vicinity of the cone tip, as already mentioned above, the sharp edge of the magnetized surface generally leads to a high magnetic flux density [40]. This implies that when the cone becomes sharper, a stronger stray field and correspondingly a stronger field gradient is found near its tip. However, for steeper cones, the cone surface grows more parallel to the external vertical field. This reduces the demagnetization of the Fe cones, which also reduces the stray field and thus the magnetic gradient near the cones. For more

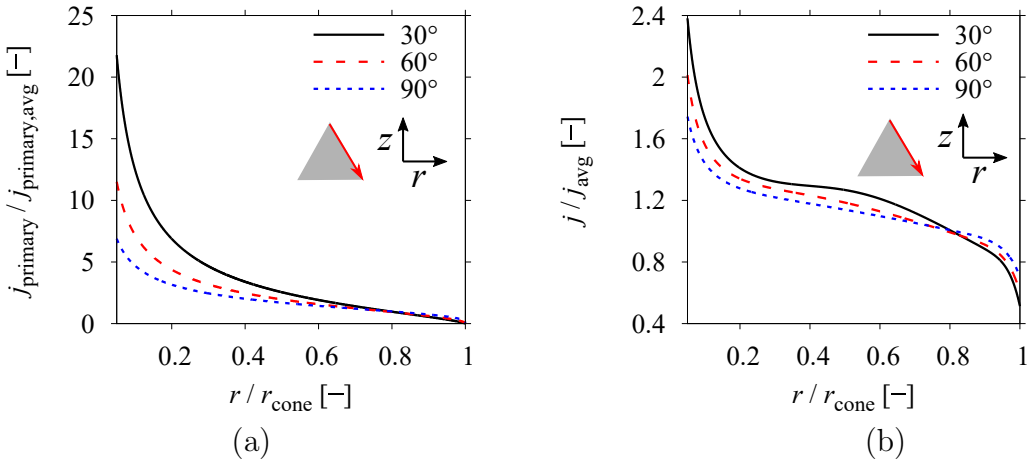

Figure 8: (a) Normalized primary current density and (b) normalized current density (No magnetic field, no convection) at cones of different tip angles α_{tip} after 10 s of deposition. $j_{\text{cathode,avg}} = 16$ mA/cm^2. The horizontal axis shows the radial surface coordinate normalized by the cone radius r_{cone}.

details on the magnetization of ferromagnetic surfaces in external magnetic fields, we refer to [40]. Due to the two opposite effects mentioned, the intermediate cone tip angle of 60° presented in Fig. 9 yields the strongest amplitudes of B and $B\nabla B$ near the tip. The strongest influence of the magnetic gradient force on the deposition might further be expected to be found at intermediate cone tip angles.

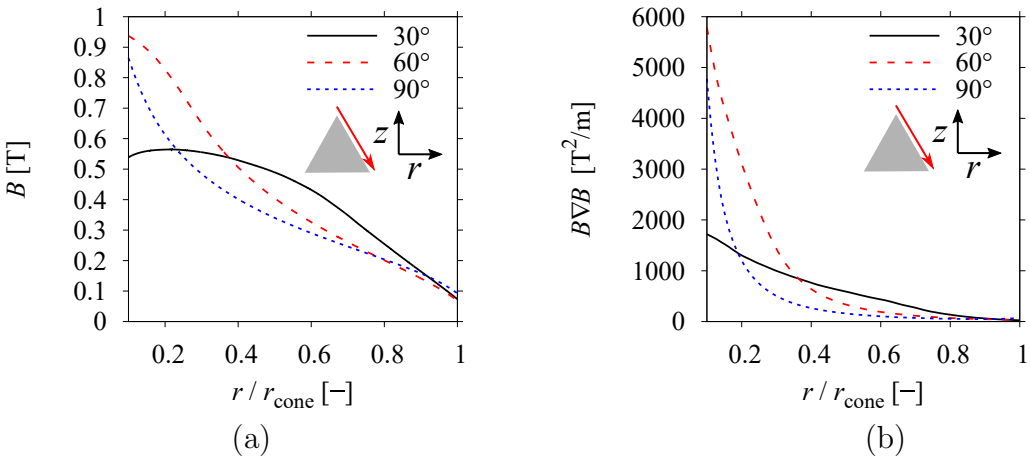

Figure 9: Magnitudes of (a) the magnetic flux density B and (b) the magnetic gradient term $B\nabla B$ along a monitoring line parallel and near (distance 35 μm) to the slanted surface of Fe cones of different tip angles. $B_0 = 200$ mT. The horizontal axis shows the radial surface coordinate normalized by the cone radius r_{cone}.

Eventually, the simulation of the deposition process at copper and iron cones of different shapes, Fig. 10, shows the distribution of the copper ion species and the meridional velocity vectors obtained after a deposition time of 10 s. For the copper cones, the downward secondary flow driven by $\boldsymbol{f}_{\mathbf{L}}$ is strongest for the steep cone of $\alpha_{\text{tip}} = 30°$ and weakest for the flat cone of $\alpha_{\text{tip}} = 90°$. As the magnetic field remains unchanged, this is in line with the behavior of the current densities shown in Fig. 8. Furthermore, although not shown in detail, a larger region with horizontal components of the current density exists near steeper cones, as the vectors must

become normal to the cone surface. All this compensates for the closer proximity of the cone surface to the symmetry axis, which reduces the azimuthal momentum delivered by $\boldsymbol{f}_{\mathbf{L}}$. For the steep cone, the concentration boundary layer rising from below is forced to separate from the cone surface slightly below the tip due to the strong downward flow, locally reducing the thickness of the boundary layer. The flatter the cone becomes, the weaker the downward flow caused by $\boldsymbol{f}_{\mathbf{L}}$, while the concentration boundary layer passes the cone tip and continues to rise freely. This leads to a thicker concentration boundary layer near the tip of the cone, as observed also experimentally for an intermediate tip angle in [1]. The plume-like shape of the tip of the separated concentration boundary layer is similar to the behavior of the temperature in free thermal convection [51].

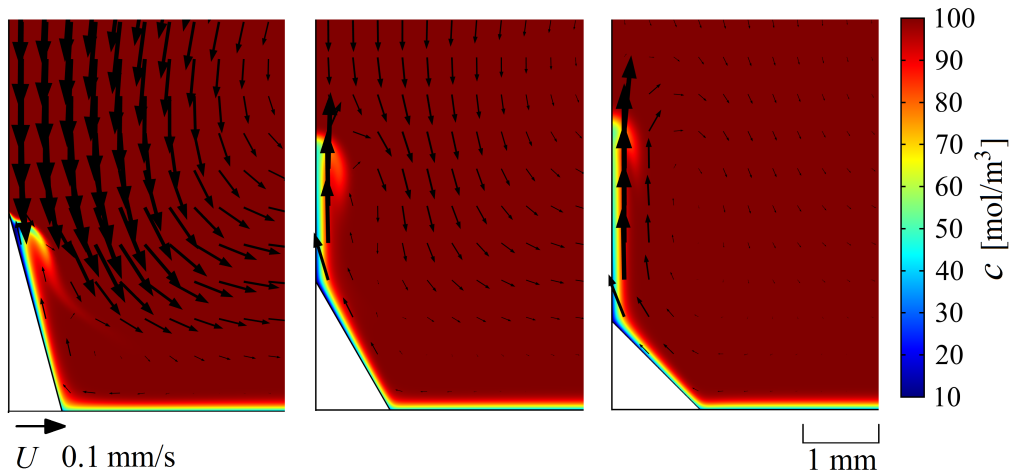

(a) Cu $t = 10$ s

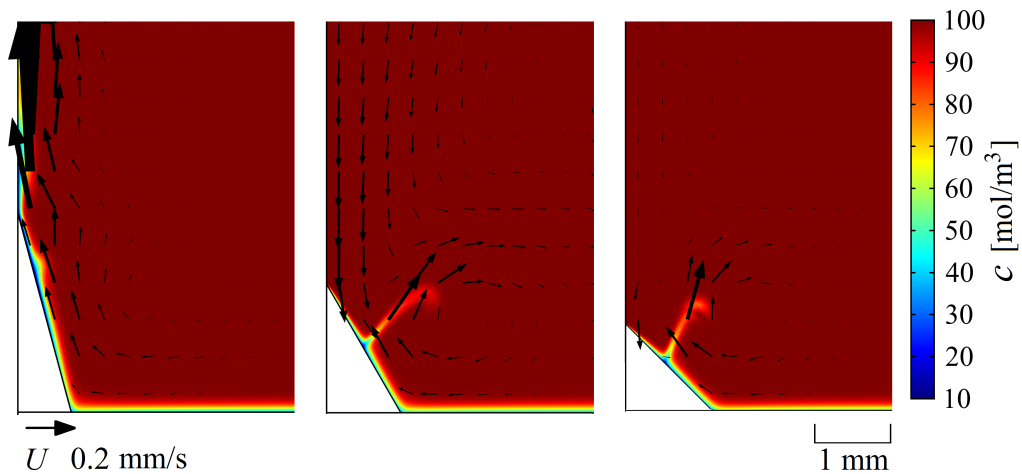

(b) Fe $t = 10$ s

Figure 10: Color surface of the concentration near (a) Cu and (b) Fe cones after 10 s deposition time ($j_{\mathrm{cathode,avg}} = 16$ mA/cm^2, $B_0 = 200$ mT). Black arrows represent the meridional velocity vectors. Cone tip angles from left to right: 30°, 60°, 90°.

For the steep iron cone, unlike the case of copper, the concentration boundary layer quickly rises vertically; its tip has already crossed the upper boundary of the region shown. This can be understood from Fig. 3, which shows a smaller region of azimuthal flow driven by $\boldsymbol{f}_{\mathbf{L}}$ compared to a copper cone. This results in

a correspondingly weaker secondary downward flow. The magnetic gradient force is also weakest for steep cones, as can be inferred from Fig. 9. Thus, the magnetic forces here are not strong enough to generate a downward flow. However, the interplay with buoyancy results in slight variations in the thickness of the rising boundary layer. For flatter iron cones, a downward flow towards the cone can be observed, which is stronger at $\alpha_{\text{tip}} = 60°$ compared to $\alpha_{\text{tip}} = 90°$, in full agreement with the discussion on the magnetic gradient term shown in Fig. 9. Compared to the copper cones discussed above, it can be concluded that this flow is mainly forced by $\boldsymbol{f}_{\nabla\mathbf{B}}$. As already discussed above, for $\alpha_{\text{tip}} = 60°$ the concentration boundary layer separates from the cone at half its height. This is also observed in the case of the flat cone, where the weaker influence of $\boldsymbol{f}_{\nabla\mathbf{B}}$ is balanced by the comparably weaker influence of $\boldsymbol{f}_{\mathbf{g}}$.

In order to evaluate the cumulative influence of the magnetic forces on the deposition, in Fig. 11 we compare the deposit thickness obtained after a deposition period of 10 s at the copper and iron cones of different shapes. In the absence of a magnetic field, as discussed above (see Fig. 8), at steep cones the natural support for further cone growth is most pronounced. When a magnetic field is applied, at steep cones the Lorentz force considerably enhances growth near the tip of the copper cone, whereas at the iron cone the support of the magnetic field for cone growth is comparably small. The intermediate tip angle of 60° was already discussed above, see Fig. 6. For the flat cone, the situation is opposite to the steep cone. The influence of $\boldsymbol{f}_{\mathbf{L}}$ at the copper cone is negligible, whereas a profound enhancement of cone growth at the iron cone can be reported, mainly due to $\boldsymbol{f}_{\nabla\mathbf{B}}$.

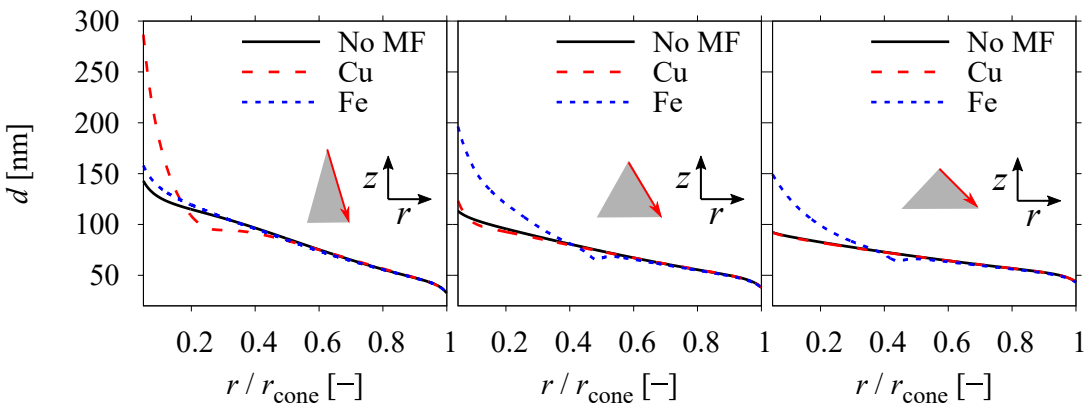

Figure 11: Deposit thickness on cones of tip angles 30°(left), 60°(middle) and 90°(right) after 10 s of deposition for the case without a magnetic field (no MF) and for Cu and Fe cones with a magnetic field ($j_{\text{cathode,avg}} = 16$ mA/cm^2, $B_0 = 200$ mT). The horizontal axis shows the radial surface coordinate normalized by the cone radius r_{cone}. The case of 60° is reprinted from Fig. 6 for comparison.

Table 4 summarizes the relative enhancement of the deposit thickness at the tip of the Cu and Fe cones compared to the case without a magnetic field after a deposition time of 10 s. It can be concluded that cone growth at diamagnetic cones supported by the action of $\boldsymbol{f}_{\mathbf{L}}$ works best for cones of a sharp shape. However, as

the support at flat cones seems to be negligible, the benefit of magnetic fields for the further development of early flat surface elevations seems rather limited.

For ferromagnetic cones, a promising enhancement of the deposit thickness was found for all the cone shapes studied here, mainly caused by the magnetic gradient force. The supporting effect was found to be the greatest with intermediate tip angles and to be moderate only in the case of steep cones. As can be seen from Fig. 11, when starting from a flat surface elevation, cone growth accelerates during deposition as the cone tip angle becomes smaller. The cone continues to grow and to become sharper. However, as soon as the optimum intermediate tip angle associated with the strongest support from the magnetic gradient force is passed, this sharpening slows down.

Table 4: Enhancement of the deposit thickness at the Cu and Fe cone tips compared to the case without a magnetic field after 10 s deposition time ($\alpha_{\text{tip}} = 30°, 60°, 90°$, $j_{\text{cathode,avg}} = 16$ mA/cm^2, $B_0 = 200$ mT).

Cone tip angle	Cu	Fe
30°	+93%	+10%
60°	+9%	+73%
90°	≈ 0	+62%

3.3. Influence of neighboring cones

Depending on the distance between adjacent cones, the flow forced at each single cone may be affected by the flow originating from its neighbors. Thus, mass transfer might also change. We therefore now extend our investigation to take into consideration the influence of neighboring cones. We first consider regular arrangements of cones on a quadratic lattice as shown in Fig. 2(c). These investigations correspond to Step 2 of the simulation methodology mentioned earlier.

As a result of the 3D simulations performed, Fig. 12 shows the horizontal components of the electrolyte velocity in a horizontal plane above the cathode touching the tips of copper cones. A square with four neighboring cones is shown, and the distance between the cone centers is varied from 5 to 1.5 cone diameters d_{cone} (see Fig. 2). At the large cone distance, a strong azimuthal flow in an anticlockwise direction is clearly visible, driven by $\boldsymbol{f}_{\mathbf{L}}$. As known from the single cone studies, this flow extends in a radial direction far beyond the cone radius (see Fig. 3). In the outer region close to half the cone distance, the neighbor influence becomes visible as a deformation of the circular shape of the azimuthal velocity contours towards a square. At half of the distance between the cones, the horizontal velocity is considerably reduced, as the two azimuthal flows are in opposite directions and hamper each other. When the distance between the cones is reduced, this damping influence increases, as seen from the lower amplitude of the azimuthal flow. At the same time, small clockwise-rotating vortices are formed at the four vertical edges of the

computational domain (most clearly visible in the center of the squares shown in Fig. 12), the amplitude of which is weak in comparison to the primary flow.

Fig. 13 shows the corresponding vertical velocity components in the vertical plane across the center of the copper cone. Because of symmetry, the results in x or y direction are identical. As the primary rotational flow is slowed down when the cones grow closer to each other, the secondary downward flow forced by $\boldsymbol{f}_{\mathbf{L}}$ also gets correspondingly weaker and has nearly disappeared at the small cone distance of $1.5\,d_{\text{cone}}$. Thus, the support of cone growth in a magnetic field is weakened as the area density of the cones grows.

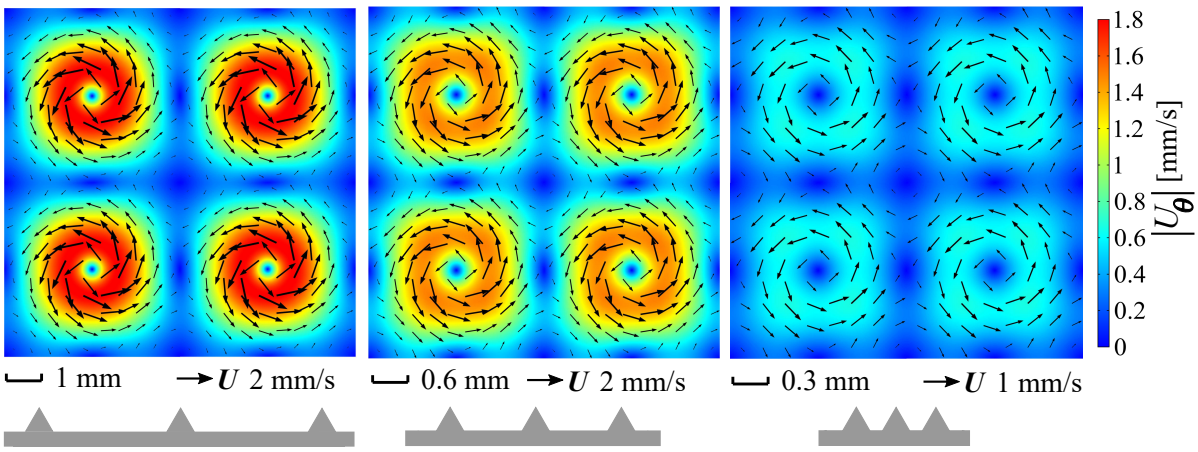

Figure 12: Horizontal velocity in a horizontal plane touching the tips of the neighboring copper cones obtained from 3D simulations after a deposition time of 5 s (α_{tip} =60°, $j_{\text{cathode,avg}}$ = 8 mA/cm^2, B_0 = 400 mT). Black arrows of the horizontal velocity vectors and color contours of the azimuthal velocity component. The cone distance in units of d_{cone} shrinks from left to right (5, 3, 1.5). Note that the scale of length and of the velocity vectors changes from left to right.

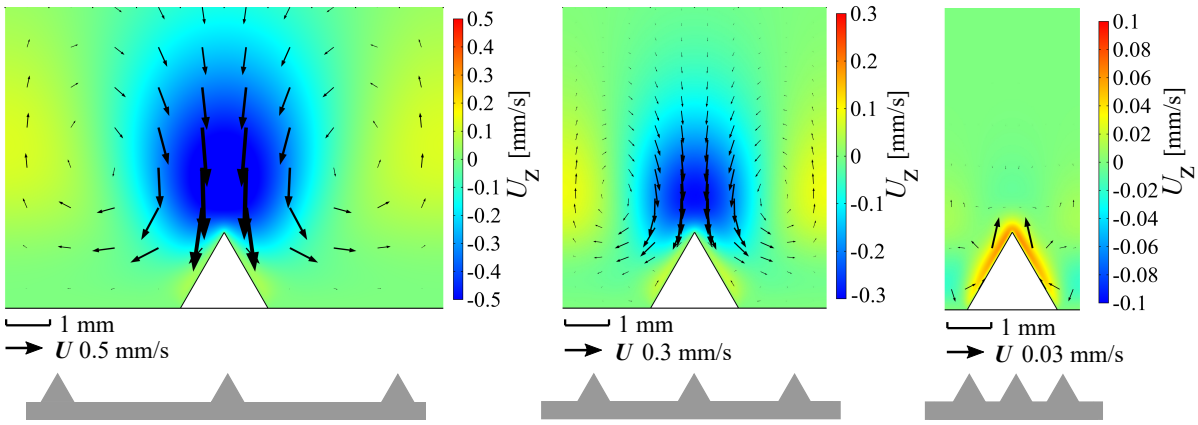

Figure 13: Vertical velocity on the vertical plane across the center of the copper cone in x direction obtained from 3D simulations after a deposition time of 5 s (α_{tip} =60°, $j_{\text{cathode,avg}}$ = 8 mA/cm^2, B_0 = 400 mT). The cone distance in units of d_{cone} shrinks from left to right (5, 3, 1.5). Black arrows represent the velocity vectors, the scale of which changes from left to right.

It should be mentioned that the computational effort for these 3D simulations is great and would be even greater for the iron cones, where steep gradients in the magnetic field near the surface of the cones additionally need to be accurately resolved. A validation of the axisymmetric 2D approach denoted as Step 3 in Section

2.1 could allow the computational effort for these simulations to be reduced considerably. This is motivated by the persistence of strong axisymmetry at a shrinking cone distance, as shown in Fig. 12. We therefore next present a comparison of results obtained by the 3D method and by the axisymmetric 2D approach for Cu cones. Fig. 14(a) shows the magnitude of the maximum azimuthal velocity of the primary flow versus the cone distance after a deposition time of 5 s. The results of the 3D and 2D approaches for the Cu case are close and follow the trend mentioned above of the azimuthal rotational flow becoming weaker if the cone distance is reduced. Fig. 14(b) shows the vertical velocity measured slightly above the cone tip. Again, both 3D and 2D results in the case of Cu are close and show that the downward flow velocity weakens. In both cases, the 2D axisymmetric results slightly overstate the damping influence compared to the 3D results, which is reasonable, as immediately neighboring cones are assumed to be found at every angular position compared to only four immediately neighboring cones in the 3D case. Nevertheless, the axisymmetric 2D approach proves to be an accurate and effective means of studying the neighbor influence. The intrinsic slight overestimation of the neighbor influence allows upper boundaries for the damping neighbor effect to be found quickly. All results presented in the following, including the cases of the iron cones, are therefore obtained by 2D simulations.

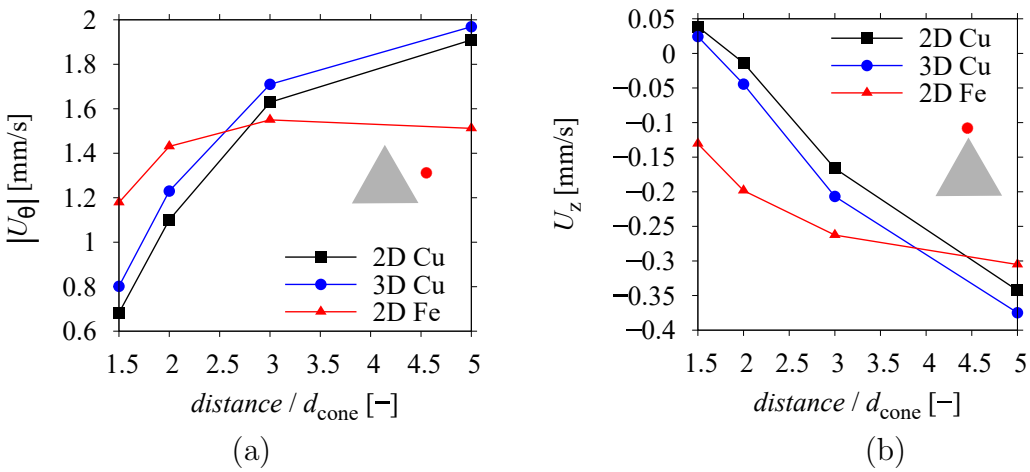

Figure 14: (a) Magnitude of the maximal azimuthal velocity, $|\,U_\theta\,|$, and (b) the vertical velocity U_z at 0.3 mm above the cone tip versus cone distance for Cu (2D and 3D results) and Fe cones (2D results) after 5 s of deposition (α_{tip} =60°, $j_{\text{cathode,avg}} = 8$ mA/cm^2, $B_0 = 400$ mT).

For the iron cones, unlike the copper cones, varying the distance between the cones can change their magnetization and thus the magnetic field. Fig. 15 shows the magnitudes of B and $B\nabla B$ near the cone surface for different cone distances. When the neighboring cones grow closer, the magnetic field near a magnetized Fe cone becomes slightly weaker. Regarding the magnetic field gradient term, reducing the distance to the neighbor cones has a small influence near the lower half of the iron cone only.

As shown in Fig. 14, shrinking the cone distance has a much weaker effect on the

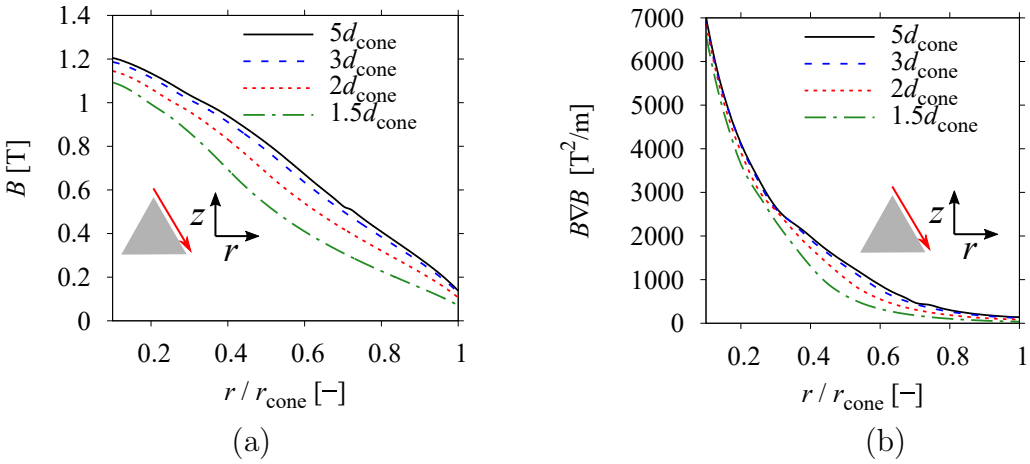

Figure 15: Magnitudes of (a) the magnetic flux density, B, and (b) the magnetic gradient term, $B\nabla B$, along a monitoring line parallel to the slanted cone surface (distance to the cone surface: 35 μm) for different distances between the Fe cones (α_{tip} =60°, $j_{\text{cathode,avg}} = 8$ mA/cm^2, $B_0 = 400$ mT). The horizontal axis shows the radial surface coordinate normalized by the cone radius r_{cone}.

electrolyte flow near the iron cones compared to the copper cones. The maximum azimuthal velocity shown on the left (a) remains nearly constant and eventually decreases only slightly towards a distance of 1.5 d_{cone}. The comparably weak neighbor effects on the azimuthal flow are related to the bending of the magnetic field near the iron cones. More details are given in SI. The vertical velocity shown on the right (b) and depicted slightly above the cone tip, contrary to the Cu cones, remains negative even at the shortest distance of 1.5 d_{cone} shown. As the cone distance shrinks, this downward flow is also weakened due to the continuity of the flow, as the vertical backflow in the narrow gap between the cones is in the opposite direction. But the slowing of this flow is moderate only. The obvious reason is that the downward flow caused by $\boldsymbol{f}_{\nabla\mathbf{B}}$ is driven near the cones. This is unlike the downward flow caused by $\boldsymbol{f}_{\mathbf{L}}$, which is a result of the primary azimuthal flow driven in a radially extended region. Thus, the supporting influence of $\boldsymbol{f}_{\nabla\mathbf{B}}$ for cone growth can be expected to be less affected by neighboring cones compared to $\boldsymbol{f}_{\mathbf{L}}$.

Fig. 16(a) shows the concentration and meridional flow for the Cu case at a later deposition time (13 s), at which the downward secondary flow caused by $\boldsymbol{f}_{\mathbf{L}}$ is only visible at the largest cone distance. As the distance between the cones shrinks and the secondary flow of the Lorentz force becomes weaker, the buoyant upward convection of the concentration boundary layer is enhanced. The only exception is that, as the cone distance decreases from 2 d_{cone} to 1.5 d_{cone}, the buoyant flow seems to be slightly weaker again, as seen from the height of the buoyancy plume. This might be due to stronger damping between the upward buoyant flow and the downward backflow, as the radial distance between these two flow regions also shrinks with the cone distance.

In the case of the iron cones, as shown in Fig. 16(b), unlike the Cu cones, the downward flow resulting from the two magnetic forces seems to be only slightly weakened as the cone distance shrinks. Therefore, support for cone growth by the

magnetic field can be expected in all cases. The weakening of the downward flow results in a slight increase in the height at which the concentration boundary layer leaves the cone, as discussed above in the case of single iron cones. In all cases, the concentration boundary layer at the Fe cones exhibits further periodic thickness variations along the cone at a length scale much smaller than the cone diameter. These are mainly caused by the action of the magnetic gradient force $\boldsymbol{f}_{\nabla \mathbf{B}}$. The position of the departing jet of depleted electrolyte can also be understood as the most unstable location of the boundary layer [38, 52].

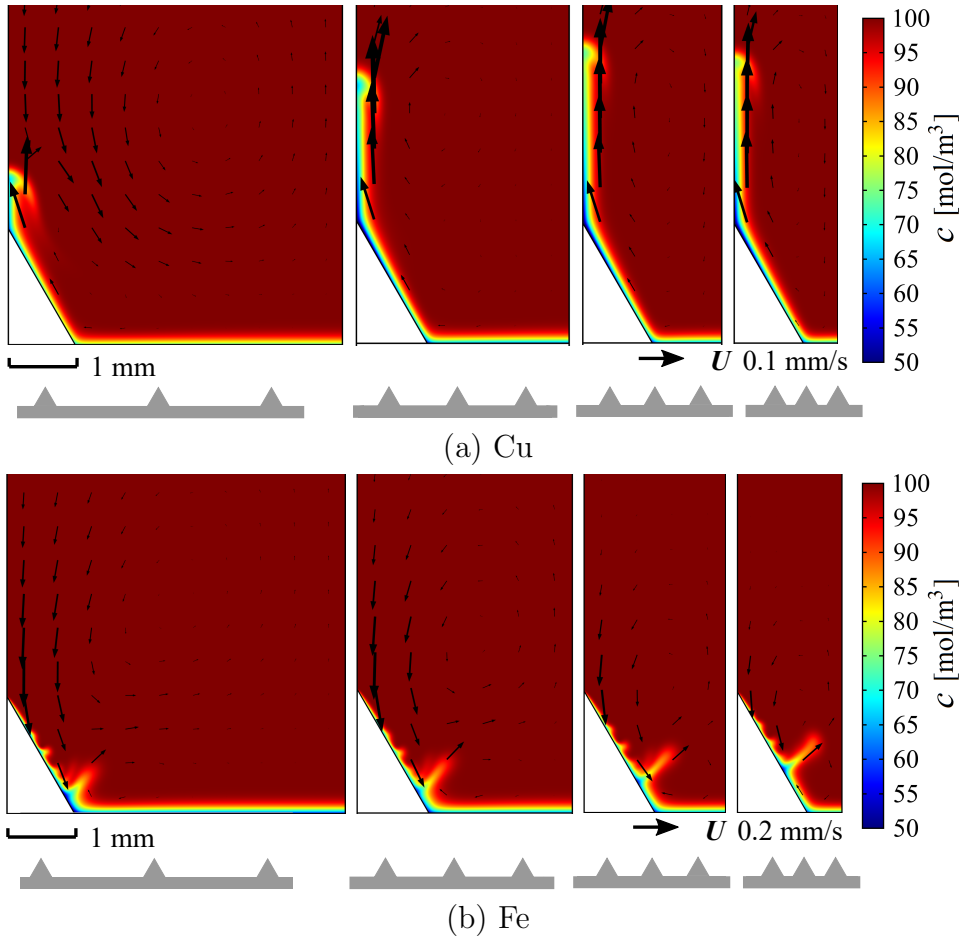

Figure 16: Species concentration (color surface) and meridional velocity vectors (black arrows) for (a) Cu and (b) Fe cones at different distances after 13 s of deposition. (α_{tip} =60°, $j_{\text{cathode,avg}} = 8$ mA/cm^2, $B_0 = 400$ mT). The cone distance in unit of d_{cone} shrinks from left to right (5, 3, 2, 1.5). Note that the scales of the velocity vectors for Cu and Fe cones are different.

Finally, Fig. 17 shows the deposit thickness obtained for the smallest cone distance of $1.5\,d_{\text{cone}}$ investigated. A longer deposition time of 50 s is also considered. As can be seen, for the Cu cones, the structuring effect due to $\boldsymbol{f}_{\mathbf{L}}$ is negligible when compared to the case without a magnetic field, which is in accordance with the buoyancy-dominated flow pattern shown in Fig. 16(a). For the iron cones, however, the support for cone growth by the magnetic field, i.e. mainly by $\boldsymbol{f}_{\nabla \mathbf{B}}$, is clearly visible.

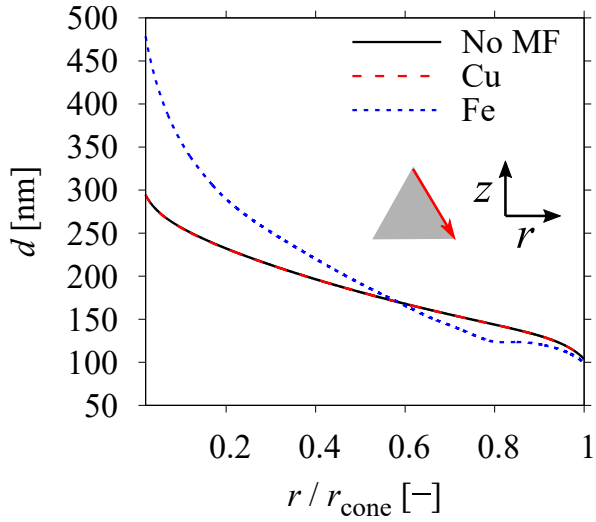

Figure 17: Deposit thickness along the cone surface for the case without a magnetic field (No MF) and for Cu and Fe cones in a vertical magnetic field after 50 s of deposition ($\alpha_{\mathrm{tip}} = 60^\circ$, $j_{\mathrm{cathode,avg}} = 8$ mA/cm^2, $B_0 = 400$ mT). The distance to neighboring cones is $1.5\,d_{\mathrm{cone}}$, the horizontal axis shows the radial surface coordinate normalized by the cone radius r_{cone}.

4. Conclusions

The analytical and numerical results of this work offer an insight into the basic effects of a vertical magnetic field on electrodeposition at conically shaped metal electrodes. The focus is on ferromagnetic conical structures of mm size. We show that cone growth can be supported by the flow driven by the Lorentz force and the magnetic gradient force that enriches the electrolyte near the cone, and thus enhances the local mass transfer.

As the cathode is assumed to be placed at the bottom of the electrochemical cell, the beneficial magnetic effects are counteracted by solutal buoyancy arising from the electrode reaction. The Lorentz force is surpassed by the buoyancy force after the first few seconds of the deposition. In comparison, the magnetic gradient force enabled by the magnetization of the ferromagnetic cones provides stronger support for cone growth, thereby often dominating over buoyancy. In general, the flow is caused by the rotational parts of both magnetic gradient force and buoyancy force.

We studied cones with different tip angles and found that the sharpest cone yields the strongest Lorentz force, while an intermediate cone tip angle generates the highest magnetic gradient force. As the evolution of the conical structures usually develops from flat surface elevations, it could be anticipated that the growth of ferromagnetic cones may be slow at the beginning, followed by an acceleration of the growth speed until an optimum shape is approached with respect to the supporting effect. Later on, growth will continue at a lower speed.

When the neighboring cones come closer to each other, the azimuthal flow caused by the Lorentz force is strongly damped. In comparison, the meridional flow caused by the magnetic gradient force is less affected, as it is driven in the close vicinity of

the cone surface.

Our results demonstrate the superiority of the magnetic gradient force in terms of supporting the structured electrodeposition in a magnetic field. We expect this superiority to enhance further when extending the investigation towards the micro- and nanometer scale, where larger field gradients are to be expected. This may encourage further research on magnetic field assisted electrodeposition as a simple and efficient method for synthesizing micro- and nano-structured ferromagnetic surfaces.

Acknowledgments

We would like to thank Xuegeng Yang, Margitta Uhlemann, Piotr Zabinski and Katarzyna Skibinska for fruitful discussions. Financial support by Deutsche Forschungsgemeinschaft, grant no. 381712986 is gratefully acknowledged.

References

[1] M. Huang, G. Marinaro, X. Yang, B. Fritzsche, Z. Lei, M. Uhlemann, K. Eckert, G. Mutschke, Mass transfer and electrolyte flow during electrodeposition on a conically shaped electrode under the influence of a magnetic field, Journal of Electroanalytical Chemistry 842 (2019) 203–213.

[2] T. Hang, A. Hu, H. Ling, M. Li, D. Mao, Super-hydrophobic nickel films with micro-nano hierarchical structure prepared by electrodeposition, Applied Surface Science 256 (2010) 2400–2404.

[3] T. Mouterde, G. Lehoucq, S. Xavier, A. Checco, C. T. Black, A. Rahman, T. Midavaine, C. Clanet, D. Quéré, Antifogging abilities of model nanotextures, Nature materials 16 (2017) 658–663.

[4] H. Zhang, S. Hwang, M. Wang, Z. Feng, S. Karakalos, L. Luo, Z. Qiao, X. Xie, C. Wang, D. Su, et al., Single atomic iron catalysts for oxygen reduction in acidic media: particle size control and thermal activation, Journal of the American Chemical Society 139 (40) (2017) 14143–14149.

[5] L. Liu, A. Corma, Metal catalysts for heterogeneous catalysis: from single atoms to nanoclusters and nanoparticles, Chemical reviews 118 (10) (2018) 4981–5079.

[6] G. B. Darband, M. Aliofkhazraei, S. Shanmugam, Recent advances in methods and technologies for enhancing bubble detachment during electrochemical water splitting, Renewable and Sustainable Energy Reviews 114 (2019) 109300.

[7] N. Wang, T. Hang, D. Chu, M. Li, Three-dimensional hierarchical nanostructured Cu/Ni–Co coating electrode for hydrogen evolution reaction in alkaline media, Nano-micro letters 7 (2015) 347–352.

[8] G. B. Darband, M. Aliofkhazraei, S. Hyun, A. S. Rouhaghdam, S. Shanmugam, Electrodeposition of Ni–Co–Fe mixed sulfide ultrathin nanosheets on ni nanocones: a low-cost, durable and high performance catalyst for electrochemical water splitting, Nanoscale 11 (35) (2019) 16621–16634.

[9] S. Arai, M. Ozawa, M. Shimizu, Communication micro-scale columnar architecture composed of copper nano sheets by electrodeposition technique, Journal of The Electrochemical Society 164 (2) (2016) D72–D74.

[10] G. B. Darband, M. Aliofkhazraei, A. S. Rouhaghdam, Three-dimensional porous Ni-CNT composite nanocones as high performance electrocatalysts for hydrogen evolution reaction, Journal of Electroanalytical Chemistry 829 (2018) 194–207.

[11] A. K. Singh, D. Sarkar, Enhanced light absorption and charge carrier management in core-shell Fe_2O_3@Nickel nanocone photoanodes for photoelectrochemical water splitting, ChemCatChem 11 (24) (2019) 6355–6363.

[12] K. Aoki, Theory of current distribution at a conical electrode under diffusion control with time dependence, Journal of electroanalytical chemistry and interfacial electrochemistry 281 (1990) 29–40.

[13] R. Aogaki, K. Fueki, T. Mukaibo, Application of magnetohydrodynamic effect to the analysis of electrochemical reactions 1. mhd flow of an electrolyte solution in an electrode-cell with a short rectangular channel, Denki Kagaku oyobi Kogyo Butsuri Kagaku 43 (9) (1975) 504–508.

[14] A. Bund, S. Koehler, H. Kuehnlein, W. Plieth, Magnetic field effects in electrochemical reactions, Electrochimica Acta 49 (1) (2003) 147–152.

[15] G. Mutschke, A. Hess, A. Bund, J. Fröhlich, On the origin of horizontal counter-rotating electrolyte flow during copper magnetoelectrolysis, Electrochimica Acta 55 (5) (2010) 1543–1547.

[16] Y. Zhang, B. Yuan, L. Li, C. Wang, Edge electrodeposition effect of cobalt under an external magnetic field, Journal of Electroanalytical Chemistry (2020) 114143.

[17] S. Mühlenhoff, G. Mutschke, M. Uhlemann, X. Yang, S. Odenbach, J. Fröhlich, K. Eckert, On the homogenization of the thickness of cu deposits by means of mhd convection within small dimension cells, Electrochemistry Communications 36 (2013) 80–83.

[18] M. Najminoori, A. Mohebbi, K. Afrooz, B. G. Arabi, The effect of magnetic field and operating parameters on cathodic copper winning in electrowinning process, Chemical Engineering Science 199 (2019) 1–19.

[19] K. Nishikawa, T. Saito, H. Matsushima, M. Ueda, Holographic interferometric microscopy for measuring Cu^{2+} concentration profile during cu electrodeposition in a magnetic field, Electrochimica Acta 297 (2019) 1104–1108.

[20] H. A. Murdoch, D. Yin, E. Hernández-Rivera, A. K. Giri, Effect of applied magnetic field on microstructure of electrodeposited copper, Electrochemistry Communications 97 (2018) 11–15.

[21] P. Żabiński, K. Mech, R. Kowalik, Electrocatalytically active Co–W and Co–W–C alloys electrodeposited in a magnetic field, Electrochimica Acta 104 (2013) 542–548.

[22] K. Shen, Z. Wang, X. Bi, Y. Ying, D. Zhang, C. Jin, G. Hou, H. Cao, L. Wu, G. Zheng, et al., Magnetic field–suppressed lithium dendrite growth for stable lithium-metal batteries, Advanced Energy Materials 9 (20) (2019) 1900260.

[23] A. Wang, Q. Deng, L. Deng, X. Guan, J. Luo, Eliminating tip dendrite growth by Lorentz force for stable lithium metal anodes, Advanced Functional Materials 29 (25) (2019) 1902630.

[24] J. A. Koza, M. Uhlemann, A. Gebert, L. Schultz, Desorption of hydrogen from the electrode surface under influence of an external magnetic field, Electrochemistry communications 10 (9) (2008) 1330–1333.

[25] J. A. Koza, S. Mühlenhoff, P. Żabiński, P. A. Nikrityuk, K. Eckert, M. Uhlemann, A. Gebert, T. Weier, L. Schultz, S. Odenbach, Hydrogen evolution under the influence of a magnetic field, Electrochimica Acta 56 (6) (2011) 2665–2675.

[26] D. Fernández, Z. Diao, P. Dunne, J. Coey, Influence of magnetic field on hydrogen reduction and co-reduction in the $Cu/CuSO_4$ system, Electrochimica acta 55 (28) (2010) 8664–8672.

[27] H. Liu, Q. Hu, L. Pan, R. Wu, Y. Liu, D. Zhong, Electrode-normal magnetic field facilitating neighbouring electrochemical bubble release from hydrophobic islets, Electrochimica Acta 306 (2019) 350–359.

[28] K. Tschulik, R. Sueptitz, J. Koza, M. Uhlemann, G. Mutschke, T. Weier, A. Gebert, L. Schultz, Studies on the patterning effect of copper deposits in magnetic gradient fields, Electrochimica Acta 56 (1) (2010) 297–304.

[29] P. Dunne, J. Coey, Patterning metallic electrodeposits with magnet arrays, Physical Review B 85 (22) (2012) 224411.

[30] G. Mutschke, A. Bund, On the 3D character of the magnetohydrodynamic effect during metal electrodeposition in cuboid cells, Electrochemistry Communications 10 (4) (2008) 597–601.

[31] L. M. Monzon, J. M. D. Coey, Magnetic fields in electrochemistry: The Lorentz force. a mini-review, Electrochemistry Communications 42 (2014) 38–41.

[32] J. Coey, F. Rhen, P. Dunne, S. McMurry, The magnetic concentration gradient force - is it real?, Journal of solid state electrochemistry 11 (6) (2007) 711–717.

[33] G. Mutschke, K. Tschulik, T. Weier, M. Uhlemann, A. Bund, J. Fröhlich, On the action of magnetic gradient forces in micro-structured copper deposition, Electrochimica Acta 55 (28) (2010) 9060–9066.

[34] G. Mutschke, K. Tschulik, M. Uhlemann, A. Bund, J. Fröhlich, Comment on magnetic structuring of electrodeposits, Physical review letters 109 (2012) 229401.

[35] M. Uhlemann, K. Tschulik, A. Gebert, G. Mutschke, J. Fröhlich, A. Bund, X. Yang, K. Eckert, Structured electrodeposition in magnetic gradient fields, The European Physical Journal Special Topics 220 (2013) 287–302.

[36] H. Danan, A. Herr, A. Meyer, New determinations of the saturation magnetization of nickel and iron, Journal of Applied Physics 39 (2) (1968) 669–670.

[37] J. Newman, K. E. Thomas-Alyea, Electrochemical systems, 3rd Edition, John Wiley & Sons, 2012.

[38] A. Bejan, Convection heat transfer, 3rd Edition, John wiley & sons, 2013.

[39] T. Weier, D. Baczyzmalski, J. Massing, S. Landgraf, C. Cierpka, The effect of a Lorentz-force-driven rotating flow on the detachment of gas bubbles from the electrode surface, International Journal of Hydrogen Energy 42 (33) (2017) 20923–20933.

[40] J. D. Jackson, Classical electrodynamics, 3rd Edition, John Wiley and Sons, 1999.

[41] COMSOL Multiphysics Documentation Suite V 5.5, COMSOL Inc., Burlington, MA 01803, USA (2019).

[42] J. Coey, New permanent magnets; manganese compounds, Journal of Physics: Condensed Matter 26 (6) (2014) 064211.

[43] D. Koschichow, G. Mutschke, X. Yang, A. Bund, J. Fröhlich, Numerical simulation of the onset of mass transfer and convection in copper electrolysis subjected to a magnetic field, Russian Journal of Electrochemistry 48 (7) (2012) 682–691.

[44] C. Akilan, T. Chen, T. Vielma, P. M. May, G. Senanayake, G. Hefter, Volumes and heat capacities of cobalt(II), nickel(II), and copper(II) sulfates in aqueous solution, Journal of Chemical & Engineering Data 65 (9) (2020) 4575–4581.

[45] P. Novotny, O. Sohnel, Densities of binary aqueous solutions of 306 inorganic substances, Journal of Chemical and Engineering Data 33 (1) (1988) 49–55.

[46] D. R. Lide, CRC handbook of chemistry and physics, Vol. 85, CRC press, 2004.

[47] X. Yang, S. Mühlenhoff, P. A. Nikrityuk, K. Eckert, The initial transient of natural convection during copper electrolysis in the presence of an opposing Lorentz force: current dependence, The European Physical Journal Special Topics 220 (1) (2013) 303–312.

[48] C. N. Singman, Atomic volume and allotropy of the elements, Journal of Chemical Education 61 (2) (1984) 137–142.

[49] M. Matlosz, C. Creton, C. Clerc, D. Landolt, Secondary current distribution in a hull cell boundary element and finite element simulation and experimental verification, Journal of the Electrochemical Society 134 (12) (1987) 3015–3021.

[50] C. Low, E. Roberts, F. Walsh, Numerical simulation of the current, potential and concentration distributions along the cathode of a rotating cylinder hull cell, Electrochimica Acta 52 (11) (2007) 3831–3840.

[51] E. Sparrow, R. Husar, R. Goldstein, Observations and other characteristics of thermals, Journal of Fluid Mechanics 41 (4) (1970) 793–800.

[52] R. Nelson, A. Bejan, Constructal optimization of internal flow geometry in convection, Journal of heat transfer 120 (2) (1998) 357–364.